J. Fluid Mech. (1998), *vol.* 364, *pp.* 221–251. Printed in the United Kingdom

© 1998 Cambridge University Press

Dynamics of radiating cold domes on a sloping bottom

By GORDON E. SWATERS

Applied Mathematics Institute, Department of Mathematical Sciences
and Institute of Geophysics, Meteorology and Space Physics,
University of Alberta, Edmonton, T6G 2G1, Canada

(Received 19 June 1997 and in revised form 20 January 1998)

Numerical simulations of benthic gravity-driven currents along continental shelves suggest they exhibit considerable time and spatial variability and tend to organize themselves into large-scale bottom-intensified cold domes or eddies. Attempts to derive simple relations governing the evolution of the spatial moments of the mass equation for baroclinic eddies have failed because it is not clear how to express the form or wave drag stresses associated with the excited (topographic) Rossby wave field in the surrounding fluid in terms of the eddy moments. We develop a simple model for the leading-order time evolution of a cold dome configuration which initially nearly satisfies the Mory–Stern isolation constraint. As the topographic Rossby wave field in the surrounding fluid interacts with the cold dome, higher azimuthal modes are excited within the cold dome which develop into spiral-like filamentary structures on the eddy boundary. The trajectory followed by the position of the maximum height of the cold dome corresponds to sub-inertial along- and cross-slope oscillations superimposed on a mean along-slope drift (well described by the Nof velocity). Nevertheless, the theory suggests that there are no oscillations (at least to second order) in the horizontal spatial moments of the eddy height, that is, the centre of mass of the eddy moves steadily in the along- and down-slope directions (i.e. 'southwestward' relative to the topographic β-plane). The theoretical analysis is in good agreement with a nonlinear numerical simulation which we present.

1. Introduction

Continental shelves are important regions for the formation and transport of deep water masses in the ocean. These flows make an important contribution to the thermohaline circulation and thus long-term climate dynamics. Examples include the Denmark Strait overflow (Smith 1976), the migration of Antarctic Bottom Water (Whitehead & Worthington 1982), deep water formation in the Adriatic Sea (Zoccolotti & Salusti 1987), and deep water replacement in the Strait of Georgia (LeBlond *et al.* 1991; Karsten, Swaters & Thomson 1995). The formation of propagating cold domes (e.g. Armi & D'Asaro 1980; Houghton *et al.* 1982; Ou & Houghton 1982; Mory, Stern & Griffiths 1987; Whitehead *et al.* 1990) is probably the result of the baroclinic instability of these currents (e.g. Jiang & Garwood 1995, 1996; Chapman & Gawarkiewicz 1995 and Gawarkiewicz & Chapman 1995). The spatial scale of these flows is, by and large, too small to be accurately resolved by the present generation of ocean general circulation models (OGCMs; see e.g. Visbeck, Marshall & Haine

https://doi.org/10.1017/S0022112098001049 Published online by Cambridge University Press

1997). It has been necessary, therefore, to parameterize their effects, such as the mass transport, in OGCMs which in turn requires understanding their dynamics.

Swaters & Flierl (1991) and Swaters (1991) developed a two-layer theory describing the baroclinic evolution of these currents. This model was based on a sub-inertial approximation to the shallow water equations in which the geostrophic pressure in the upper layer (see figure 1) was principally driven by baroclinic vortex-tube stretching and a background topographic vorticity gradient. The lower layer, while geostrophic, allowed for finite-amplitude thickness variations in order to allow for coupled front configurations in the lower layer height. The mean flow in the lower layer arises primarily due to a geostrophic balance between the Coriolis stress and the down-slope gravitational acceleration associated with a relatively dense water mass sitting directly on a sloping shelf. This model filtered out barotropic instabilities and focused on the baroclinic destabilization of density-driven currents on a sloping bottom.

Swaters (1991) examined the linear instability characteristics of these flows. For an unstable lower layer flow which has a cross-shelf-height profile shaped like a coupled front, the instabilities take the form of along-front travelling waves which preferentially amplify on the down-slope side of the coupled front and which eventually develop into down-slope propagating plumes and subsequently into along-slope propagating cold domes (Swaters 1998).

The asymmetry in the evolution of the perturbed up-slope and down-slope incroppings is a signature of the baroclinic destabilization of these currents and cannot be reproduced by a barotropic instability theory (see e.g. Griffiths, Killworth & Stern 1982; Paldor & Killworth 1987). The asymmetrical evolution of the incroppings is clearly seen in three-dimensional numerical simulations of these flows (e.g. Jiang & Garwood 1995, 1996; Chapman & Gawarkiewicz 1995 and Gawarkiewicz & Chapman 1995).

Solutions corresponding to isolated travelling cold domes were found by Swaters & Flierl (1991). These eddies are the baroclinic extensions of the reduced-gravity eddy solutions found by Nof (1983). Numerical simulations (Swaters 1998) show that these solutions are relatively long-lived (up to 40 eddy circulation times or on the order of 200–300 days for typical continental shelf parameter values) and remain remarkably coherent even though they are probably dynamically unstable (Swaters 1993).

One aspect seen in the numerical simulations described by Swaters (1998) is that, in general, the motion of these cold domes is not purely rectilinear. In particular, the trajectory followed by the position of maximum height of the cold dome which emerged in the instability simulation showed a distinct cross-slope oscillation superimposed on a dominant essentially steady along-slope drift.

This observation is easily understood in a qualitative sense as a consequence of potential vorticity conservation in the overlying fluid. In general, a field of topographic Rossby waves will be generated in the surrounding fluid as the cold dome propagates through it. Associated with the wave field will be a form or wave drag on the cold eddy which balances with the net Coriolis stress (see e.g. Flierl 1984) to produce, initially at least, down-slope (or 'southward' relative to the topographic β-plane) motion.

However, as the cold dome, which generates cyclonic relative vorticity in the upper layer, moves in the down-slope direction, the induced upper layer flow advects fluid parcels in the cross-slope directions, which, through potential vorticity conservation, acts, in turn, to advect fluid parcels back in the up-slope direction (this is precisely the mechanism behind planetary Rossby wave propagation). The principal purpose of this paper is to develop a theory for the cross-slope motion of a radiating baroclinic cold

https://doi.org/10.1017/S0022112098001049 Published online by Cambridge University Press

dome on a sloping bottom as a consequence of the dynamical interaction between the propagating cold dome and the excited external topographic Rossby wave field in the surrounding fluid.

Nof (1984) developed a barotropic model describing the oscillatory drift of cold domes. The oscillations described by Nof (1984) occur at the inertial period. The Swaters & Flierl (1991) and Swaters (1991) model corresponds to a sub-inertial approximation to the two-layer shallow water equations in which inertial and super-inertial modes have been filtered out. The oscillations we describe here are distinctly sub-inertial and owe their existence to a dynamical baroclinic interaction between the cold dome and the overlying fluid. This is a substantially different dynamical process than that modelled by Nof (1984).

Attempts to derive a simple set of relations describing the time-dependent drift of barotropic or reduced-gravity oceanographic eddies have been based on obtaining evolution equations for the horizontal spatial moments of the eddy height (e.g. Killworth 1983; Nof 1984; Cushman-Roisin, Chassignet & Tang 1990). However, in the baroclinic context, this approach fails because it has not been possible to express the form drag, i.e. baroclinic coupling, stresses in terms of the eddy moments (Cushman-Roisin *et al.* 1990) which is required to get a closed set of equations.

It appears that, in general, it is necessary to explicitly compute the full nonlinear time evolution of the surrounding topographic Rossby wave field in order to compute the form drag terms. For this reason there has been very little progress (see e.g. Flierl 1984) in deriving a simple model for determining the propagation characteristics of radiating baroclinic eddies. However, considerable insight can be achieved by examining the evolution of an initial cold dome which has a small-but-non-zero form drag associated with the exterior wave field or, equivalently, which nearly satisfies the Mory–Stern isolation constraint (Mory 1985; Mory *et al.* 1987).

In this situation, the leading-order evolution of the azimuthal components of the upper layer topographic Rossby wave field are described by linear partial differential equations. From these equations, one can explicitly determine the form drag and thereby compute the evolution characteristics of a weakly radiating cold dome.

In particular, we show that the leading-order effect of the upper layer topographic Rossby wave field is to excite azimuthally propagating anomalies within the cold dome which have a radially dependent phase speed. This leads to the development of spiral-like perturbations which leads to a distortion of the eddy boundary or incropping into spiral-like filaments. Moreover, we show that the maximum height of the cold dome, which oscillates in magnitude over time, follows a path composed of sub-inertial cross-shelf oscillations which are superimposed on an essentially steady along-shelf drift which is well described by the Nof velocity (Nof 1983). In addition, we calculate the leading-order feedback of the evolving cold dome on the upper layer topographic Rossby wave field. Finally, we present a nonlinear numerical simulation for an initially weakly radiating cold dome. There is good agreement between the principal theoretical predictions and the numerical simulation.

The plan of the paper is as follows. In the remainder of this section we briefly introduce the governing equations. In §2 we introduce the weakly radiating ansatz. In §3 we derive and solve the governing equations for the evolution of the upper layer Rossby wave field and the eddy height. In §4 we discuss the implications of the solution, focusing on the propagation velocity of the centre of mass of the eddy, the trajectory that the maximum eddy height takes (which is often diagnosed in numerical eddy generation and instability simulations) and the evolution of the spatial structure of the deforming eddy and upper layer topographic Rossby wave

https://doi.org/10.1017/S0022112098001049 Published online by Cambridge University Press

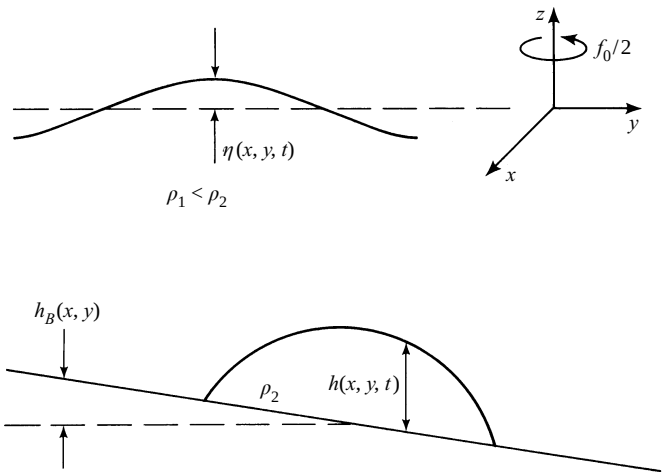


FIGURE 1. Geometry of the model used in this paper.

field. In §5 we present our numerical simulation and make a comparison between it and the theoretical analysis. In §6 we present our main conclusions.

1.1. *Model formulation*

Since the derivation of the equations has been described elsewhere (e.g. Swaters & Flierl 1991; Swaters 1991), our presentation will be brief. The physical geometry corresponds to a two-layer fluid (see figure 1) on a (northern hemisphere) f-plane with x and y the along-shore and offshore coordinates, respectively, and t is time. Alphabetical subscripts, except where indicated, represent partial differentiation.

If the geostrophic pressure in the upper layer is denoted by $\eta(x, y, t)$ and the lower layer current height, relative to the height of the variable bottom topography denoted by $h_B(x, y)$, is denoted as $h(x, y, t)$, then the non-dimensional model can be written in the form

$$\Delta\eta_t + J(h + \eta, h_B) + J(\eta, \Delta\eta) = 0, \tag{1.1}$$

$$h_t + J(\eta + h_B, h) = 0, \tag{1.2}$$

where $J(A, B) \equiv A_x B_y - A_y B_x$. Given η and h, the velocity in the upper and lower layers and the geostrophic pressure in the lower layer are given by, respectively,

$$\boldsymbol{u}_1 = \hat{\boldsymbol{e}}_3 \times \nabla\eta, \tag{1.3}$$

$$\boldsymbol{u}_2 = \hat{\boldsymbol{e}}_3 \times \nabla(\eta + h + h_B), \tag{1.4}$$

$$p = h_B + \eta + h. \tag{1.5}$$

The non-dimensional variables are related to the dimensional (asterisked) variables via the relations

$$\left.\begin{array}{lll} (x^*, y^*) = L(x, y), & t^* = (sf)^{-1} t, & h^* = sHh, \\ \boldsymbol{u}_1^* = sfL\,\boldsymbol{u}_1, & \eta^* = s(fL)^2 g^{-1}\,\eta, & \boldsymbol{u}_2^* = sg'H(fL)^{-1}\,\boldsymbol{u}_2, \\ h_B^* = sHh_B, & p^* = s\rho_2 g' H p, & \end{array}\right\} \tag{1.6}$$

where the horizontal length scale is the internal deformation radius $L = (g'H)^{1/2}/f$

https://doi.org/10.1017/S0022112098001049 Published online by Cambridge University Press

associated with the upper layer, g' is the reduced gravity and

$$s = \frac{s^* L}{H} = \frac{s^* g'/f_0}{(g'H)^{1/2}}, \tag{1.7}$$

is a scaled bottom slope parameter where s^* is the unscaled bottom slope parameter and H is the mean depth of the upper layer.

Equations (1.1) and (1.2) correspond to a $0 < s \ll 1$ asymptotic limit of the two-layer shallow water equations in which the evolution of the upper layer is quasi-geostrophic but the lower layer, while geostrophic, is not quasi-geostrophic and allows for large-amplitude thickness variations. The small-s limit may be thought of as filtering out the higher frequency dynamics associated with non-rotating gravity currents and focusing on the rotationally dominated aspects of the problem, i.e. a sub-inertial approximation.

The dimensional values associated with the above scalings depend on the local environmental parameters. For example, for the cold pool described by Houghton *et al.* (1982) and Ou & Houghton (1982), the time scale is about 7 days, the horizontal length scale is about 12 km and the lower layer velocity scale is about 2.5 cm s^{-1} (Swaters & Flierl 1991). Whereas for the deep water replacement current in the Strait of Georgia described by LeBlond *et al.* (1991), the time scale is about 11 h, the horizontal length scale is about 7 km and the lower layer velocity scale is about 18 cm s^{-1} (Karsten *et al.* 1995).

Finally, we remark that (1.1) and (1.2) possesses a non-canonical Hamiltonian formulation (Swaters 1993) in which the integrated energy, given by

$$\int\int_{\mathbb{R}^2} \nabla\eta \cdot \nabla\eta + (h + h_B)^2 - h_B^2 \, \mathrm{d}x\mathrm{d}y,$$

is an invariant of the motion, as is

$$\int\int_{\mathbb{R}^2} \Phi(\Delta\eta + h) + \Psi(h) \, \mathrm{d}x\mathrm{d}y,$$

where Φ and Ψ are arbitrary functions of their arguments. We note, for example, that choosing $\Phi(\Delta\eta + h) = (\Delta\eta + h)^2$ and $\Psi = 0$ or $\Phi = 0$ and $\Psi(h) = h$, corresponds to upper layer enstrophy or lower layer mass conservation, respectively.

2. Density-driven vortices

Nof (1983) showed that all steadily travelling solutions to the reduced gravity model (with the non-dimensionalization scheme (1.6))

$$s(\partial_t + \boldsymbol{u}_2 \cdot \nabla)\boldsymbol{u}_2 + \boldsymbol{e}_3 \times \boldsymbol{u}_2 = -\nabla(h - y),$$

$$h_t + \nabla \cdot [\boldsymbol{u}_2 h] = 0,$$

where $h_B = -y$, for which h has compact support, have a translation velocity, i.e. the Nof velocity, given by

$$\boldsymbol{c} \equiv (c_x, c_y) = (1, 0), \quad \left\{ \boldsymbol{c}^* = \left(\frac{g' s^*}{f_0}, 0 \right) \right\},$$

regardless of the shape of the eddy height. Here and henceforth the x and y subscripts on the translation velocity denote the components and not partial differentiation.

The Nof solution neglects the effects of baroclinicity. Presumably, as these dome

https://doi.org/10.1017/S0022112098001049 Published online by Cambridge University Press

structures travel through the ambient surrounding fluid there will be vortex compression/stretching and other dynamical and thermodynamical effects occurring and these will affect the evolution of the eddy and hence its translation velocity characteristics.

For example, Mory *et al.* (1987) describe rotating-tank experiments on these bottom-trapped domes. These experiments (and others e.g. Whitehead *et al.* 1990) clearly indicate that there was an appreciable azimuthal velocity field formed above the eddy in the surrounding eddy which was at least as large as the swirl velocity (i.e. the azimuthal velocity in the co-moving frame) in the eddy itself.

The importance of the upper layer can be seen in the Mory–Stern isolation constraint (Mory 1985) which, for (1.1) and (1.2), can be expressed in the form

$$\int\int_{\mathbb{R}^2} h + \eta \, \mathrm{d}x\mathrm{d}y = 0 \tag{2.1}$$

(Swaters & Flierl 1991). Since h is everywhere non-negative, the Mory–Stern isolation constraint suggests that there must be a region of cyclonic circulation over top of the travelling dome and this is what is observed in the rotating tank experiments.

Swaters & Flierl (1991) found an exact steadily travelling isolated eddy solution to (1.1) and (1.2) for constant sloping topography which travels with the Nof velocity. Assuming $h_B = -y$ and a radially-symmetric eddy of the form

$$h(r) = \begin{cases} h_s(r), & 0 \leqslant r < a \\ 0, & r \geqslant a, \end{cases} \tag{2.2}$$

assuming $h_s(a) = 0$, where a is the eddy radius and r is the radial coordinate in the co-moving frame, i.e. $r \equiv [(x - t - x_0)^2 + (y - y_0)^2]^{1/2}$ where (x_0, y_0) is arbitrary, then η, which is the solution of

$$\Delta\eta + \eta = -h, \tag{2.3}$$

subject to the radiation or 'no upstream waves' condition

$$\lim_{r\to\infty} r^{1/2}\eta = 0 \quad \text{in the sector} \quad \left|\tan^{-1}\left(\frac{y}{x}\right)\right| < \frac{\pi}{2}, \tag{2.4}$$

is given by

$$\eta(r) = \begin{cases} \eta_s(r), & 0 \leqslant r < a, \\ 0, & r \geqslant a, \end{cases} \tag{2.5}$$

where

$$\eta_s(r) = -\frac{\pi Y_0(r)}{2}\int_0^r \xi J_0(\xi) h_s(\xi)\,\mathrm{d}\xi - \frac{\pi J_0(r)}{2}\int_r^a \xi Y_0(\xi) h_s(\xi)\,\mathrm{d}\xi, \tag{2.6}$$

with the zero topographic Rossby wave condition

$$\int_0^a \xi J_0(\xi) h_s(\xi)\,\mathrm{d}\xi = 0. \tag{2.7}$$

The constraint (2.7), which quantifies the eddy radius a, arises in order to eliminate the topographic Rossby wave field in the upper layer. It can be shown (Swaters & Flierl 1991) to be equivalent to the Mory–Stern isolation constraint (2.1). Note that since this solution is radially symmetric in the co-moving frame of reference, the nonlinear Jacobian terms in the governing equations (1.1) and (1.2) are identically zero, i.e. the Swaters & Flierl solution is a fully nonlinear solution to the model. It is important to emphasize that we take the lowest non-zero value of a which satisfies (2.7) as the eddy radius (see also the comments in Swaters & Flierl 1991).

https://doi.org/10.1017/S0022112098001049 Published online by Cambridge University Press

Finally, we point out that the circulation in the upper layer is strictly cyclonic. The circulation in the cold dome is for the most part anti-cyclonic although there is a narrow band of cyclonic flow immediately adjacent to the eddy boundary (see Swaters & Flierl 1991). Swaters & Flierl (1991) have shown that it is necessary to have a region of cyclonic flow within the cold dome if the zero topographic Rossby wave constraint (2.7) is to hold.

2.1. *Radiating cold domes*

If the eddy height does not satisfy the zero topographic Rossby wave condition (2.7), then the above fails to be a physically acceptable solution since it will not satisfy the radiation condition (2.4). In and of itself, this can be remedied by adding an appropriate homogeneous solution to (2.3) (see e.g. Flierl 1984; Swaters & Flierl 1991), so that the upper layer pressure will be given by

$$\eta(r,\theta) = -\frac{\pi Y_0(r)}{2}\int_0^r \xi J_0(\xi)\, h_s(\xi)\,\mathrm{d}\xi - \frac{\pi J_0(r)}{2}\int_r^a \xi Y_0(\xi)\, h_s(\xi)\,\mathrm{d}\xi + \frac{4\mu}{\pi}\sum_{n=0}^{\infty}\frac{J_{2n+1}(r)\cos[(2n+1)\theta]}{2n+1}, \tag{2.8}$$

for $0 \leqslant r < a$, and

$$\eta(r,\theta) = \mu\left\{-Y_0(r) + \frac{4}{\pi}\sum_{n=0}^{\infty}\frac{J_{2n+1}(r)\cos[(2n+1)\theta]}{2n+1}\right\}, \tag{2.9}$$

for $r \geqslant a$, where

$$\mu \equiv \frac{\pi}{2}\int_0^a \xi J_0(\xi)\, h_s(\xi)\,\mathrm{d}\xi. \tag{2.10}$$

This expression has the property that $\eta \simeq o\left(r^{-1/2}\right)$ in the far field ahead of the travelling eddy which eliminates the wave field in the upstream direction. However, this modification still fails to be a solution of (1.1) and (1.2) because the appearance of the cosine terms in (2.8) and (2.9) will imply that the nonlinear Jacobian terms in (1.1) and (1.2) will no longer vanish. Nevertheless, substitution of (2.3), (2.8) and (2.9) into (1.1) and (1.2) shows that the error is $O(\mu)$ compared to the leading-order terms. We can exploit this fact to determine the propagation characteristics of cold domes which are initially weakly radiating, i.e. $0 < \mu \ll 1$ at $t = 0$. Note that μ will be fixed for a given eddy and it is a measure of the relative amplitude of the topographic wave field compared to the radially symmetric part of the upper layer geostrophic pressure.

One can easily see the effect of the baroclinic coupling in determining the propagation characteristics of the centre of mass of the cold dome. Assuming a linearly sloping topography of the form $h_B = -y$, then multiplying (1.2) with x and y, respectively, and integrating over the support of h, which we denote as Ω with boundary $\partial\Omega$ so that $h|_{\partial\Omega} = 0$, it follows that

$$\langle xh\rangle_t = 1 - \langle h\eta_y\rangle, \tag{2.11}$$

$$\langle yh\rangle_t = \langle h\eta_x\rangle, \tag{2.12}$$

https://doi.org/10.1017/S0022112098001049 Published online by Cambridge University Press

where

$$\langle(*)\rangle \equiv \frac{\displaystyle\int\!\!\int_{\Omega} (*)\,\mathrm{d}x\mathrm{d}y}{\displaystyle\int\!\!\int_{\Omega} h\,\mathrm{d}x\mathrm{d}y}, \tag{2.13}$$

and where we have used the fact that $\partial_t \iint_{\Omega} h\,\mathrm{d}x\mathrm{d}y = 0$.

From the view point of developing a theory for the propagation characteristics of baroclinic eddies the problem is to determine how to express the baroclinic coupling terms in (2.11) and (2.12), i.e. $\langle h\eta_y\rangle$ and $\langle h\eta_x\rangle$, back in terms of the centre of mass coordinates, i.e. $\langle xh\rangle$ and $\langle yh\rangle$. If one could do this then (2.11) and (2.12) would form a closed set of differential equations for the centre of mass and the solution would be, presumably, straightforward. However, in general, it is not known how (or even if it is possible) to do this (see e.g. the comments by Cushman-Roisin *et al.* 1990) without making additional approximations. This situation does not arise in the barotropic analogue of this problem (see e.g. Killworth 1983; Nof 1984; Cushman-Roisin *et al.* 1990).

In the situation where h and η are radially symmetric then it is trivial to see that $\langle h\eta_y\rangle = \langle h\eta_x\rangle = 0$ so that the centre of mass is steadily travelling in the along-slope direction with unit (non-dimensional) speed with no cross-slope motion whatsoever. This is, of course, exactly the property of the Swaters & Flierl (1991) solution presented earlier.

Consequently, any departure from this behaviour would seem to involve the generation of additional azimuthal harmonics (specifically $\cos(\theta)$ and $\sin(\theta)$ modes) which, in turn, suggests a complicated interaction process between an externally excited topographic Rossby wave field and the flow field within the eddy interior.

Our approach to determining the propagation characteristics of a radiating cold dome is not to try and determine a closed set of relations for the centre of mass coordinates but to explicitly compute the time evolution of the baroclinic stresses $\langle h\eta_y\rangle$ and $\langle h\eta_x\rangle$ for an initial eddy configuration which nearly satisfies the isolation constraint (2.7). In this situation the characteristic amplitude of the generated topographic Rossby wave field is sufficiently small that one can determine its evolution and its coupling with the geostrophic pressure in the eddy interior using linear partial differential equations. This we do in the next section.

3. Dynamics of weakly radiating cold domes

We begin by restricting attention to the linearly sloping bottom profile

$$h_B = -y, \tag{3.1}$$

and introduce a coordinate system moving with the Nof velocity,

$$\widetilde{x} = x - t, \quad \widetilde{y} = y, \quad \widetilde{t} = t. \tag{3.2}$$

Substitution of (3.1) and (3.2) into (1.1) and (1.2) leads to, after dropping the tildes,

$$\Delta\eta_t - [\Delta\eta + \eta + h]_x + J(\eta, \Delta\eta) = 0, \tag{3.3}$$

$$h_t + J(\eta, h) = 0. \tag{3.4}$$

Relative to the (Nof) coordinate frame (3.2), the centre of mass coordinates, denoted

https://doi.org/10.1017/S0022112098001049 Published online by Cambridge University Press

as $(X_{mass}(t), Y_{mass}(t))$, are determined by

$$X_{mass}(t) = -\int_0^t \left\{ \frac{\iint_\Omega h(x,y,\tau)\,\eta_y(x,y,\tau)\,\mathrm{d}x\mathrm{d}y}{\iint_\Omega h(x,y,\tau)\,\mathrm{d}x\mathrm{d}y} \right\} \mathrm{d}\tau, \tag{3.5}$$

$$Y_{mass}(t) = \int_0^t \left\{ \frac{\iint_\Omega h(x,y,\tau)\,\eta_x(x,y,\tau)\,\mathrm{d}x\mathrm{d}y}{\iint_\Omega h(x,y,\tau)\,\mathrm{d}x\mathrm{d}y} \right\} \mathrm{d}\tau, \tag{3.6}$$

where Ω is the support of $h(x,y,t)$ in the co-moving frame for which, on the boundary $\partial\Omega$,

$$h|_{\partial\Omega} = 0, \tag{3.7}$$

and for which, without loss of generality, we have set $X_{mass}(0) = Y_{mass}(0) = 0$. As mentioned previously, our approach is not to attempt to parameterize the expressions within the curly brackets in (3.5) and (3.6) in terms of the centre of mass coordinates or their derivatives with respect to time, but rather to explicitly evaluate these terms for an initially weakly radiating eddy for which μ is small.

If we assume a straightforward asymptotic solution to (3.3) and (3.4) of the form

$$(h,\eta) \simeq (h_0(r), \eta_0(r)) + \mu\left(\widetilde{h}(r,\theta,t), \widetilde{\eta}(r,\theta,t)\right) + O\left(\mu^2\right), \tag{3.8}$$

where (r,θ) are radial coordinates in the co-moving frame, it follows that the $O(1)$ and $O(\mu)$ problems are given by, respectively, after dropping the tildes,

$$(\Delta + 1)\,\eta_0 = -h_0, \tag{3.9}$$

$$\Delta\eta_t - \left[\cos(\theta)\,\partial_r - \frac{\sin(\theta)}{r}\partial_\theta\right](\Delta\eta + \eta + h) + \frac{\eta_{0_r}}{r}(\Delta\eta + \eta)_\theta + \frac{h_{0_r}}{r}\eta_\theta = 0, \tag{3.10}$$

$$h_t + \frac{\eta_{0_r}}{r}h_\theta - \frac{h_{0_r}}{r}\eta_\theta = 0. \tag{3.11}$$

It is convenient to write the position of the eddy boundary, i.e. $\partial\Omega$, in terms of the co-moving radial coordinates. If we denote the total eddy radius as $a(\theta,t)$, so that

$$a(\theta,t) \simeq a_0 + \mu\widetilde{a}(\theta,t) + O\left(\mu^2\right), \tag{3.12}$$

where a_0 is the initial constant eddy radius, it follows from (3.7), after Taylor expanding and inserting the expansion (3.8), that the $O(1)$ and $O(\mu)$ eddy height must satisfy, respectively, after dropping the tildes,

$$h_0(a_0) = 0, \tag{3.13}$$

$$h(a_0,\theta,t) + h_{0_r}(a_0)\,a(\theta,t) = 0. \tag{3.14}$$

The upper layer geostrophic pressure must satisfy the radiation condition (2.4) and be continuously differentiable for $(x,y) \in \mathbb{R}^2$ for all $t \geqslant 0$.

The solution to (3.9) is straightforward and can be written in the form

$$\eta_0(r) = -\frac{\pi Y_0(r)}{2}\int_0^r \xi J_0(\xi)\,h_0(\xi)\,\mathrm{d}\xi - \frac{\pi J_0(r)}{2}\int_r^{a_0} \xi Y_0(\xi)\,h_0(\xi)\,\mathrm{d}\xi. \tag{3.15}$$

It is important to note, however, that (3.15) is *not* a (spatial) uniformly valid leading-order solution for the upper layer pressure. In the far field $r \gg a_0$, $\eta_0(r) \simeq O\left(r^{-1/2}\right)$

https://doi.org/10.1017/S0022112098001049 Published online by Cambridge University Press

so that (3.15) does not satisfy the radiation condition (2.4). This non-uniformity will be eliminated when we construct the solution to (3.10) and (3.11), i.e. a uniformly valid leading-order solution requires the solution to the $O(1)$ and $O(\mu)$ problems.

The problem we examine is for an initially radially symmetric cold dome which 'nearly' satisfies (2.7), i.e.

$$0 < |\mu| \equiv \frac{\pi}{2}\left|\int_0^{a_0} rJ_0(r)\,h_0(r)\,\mathrm{d}r\right| \ll 1. \tag{3.16}$$

Thus, the appropriate initial conditions for the solutions of (3.10) and (3.11) are, respectively,

$$\eta(r,\theta,0) = \frac{4}{\pi}\sum_{n=0}^{\infty}\frac{J_{2n+1}(r)\cos[(2n+1)\theta]}{2n+1}, \tag{3.17}$$

$$h(r,\theta,0) = 0, \tag{3.18}$$

where (3.17) follows from (2.4), i.e. the sum $\eta_0(r) + \mu\eta(r,\theta,0)$ satisfies the radiation condition (2.4). It follows from (3.14) that

$$a(\theta,0) = 0. \tag{3.19}$$

In this paper we are interested in determining the leading-order feedback of the topographic Rossby wave tail on the eddy. In truth, of course, the initial value problem, in which the initial upper layer stream function was identically zero, would have the wave field spreading out from the eddy region into the far field. We are implicitly making the assumption that we can take the wave field in the upper layer as extending to infinity. This quasi-steady assumption is justified if the time scale associated with the dynamics we are interested in is long compared to the time scale of the formation of the initial topographic Rossby wave tail and if it is the near-field structure of the wave field which is most dynamically relevant for our application (which is what (3.5) and (3.6) suggest). We note that a similar quasi-steady approximation was made by Flierl (1984).

This assumption seems to be appropriate based on full nonlinear numerical simulations presented by Swaters (1998). In that paper simulations are presented corresponding to a number of different initial conditions. In one simulation, a relatively distinct and radially symmetric cold dome is seen to emerge from the baroclinic destabilization of a density-driven coupled front (see Plate 1 in Swaters 1998) on a sloping bottom. The upper layer geostrophic pressure field is composed of a field of evolving topographic Rossby waves and there is no obvious cyclonic eddy located over the cold dome. The path that the point of maximum height of the cold dome follows is (see figure 3 in Swaters 1998) composed of a dominant essentially rectilinear along-slope motion (reasonably well described by the Nof velocity) and a superimposed cross-slope periodic oscillation. The residual along-slope position of the point of maximum height of the cold dome (i.e. the along-slope position minus the dominant linear trend; see figure 3*d* in Swaters 1998) also possesses a periodic oscillatory structure which is approximately 90° out phase with the cross-slope oscillations.

In a second simulation, Swaters (1998) describes the evolution of a cold dome which is initially radially symmetric and for which (3.16) holds but where the upper layer stream function is initially zero (see Plate 4 in Swaters 1998). Thus the Mory–Stern isolation constraint (2.1) is not initially satisfied and one expects a topographic Rossby wave tail to develop. The numerical simulation clearly shows the rapid development of a topographic Rossby wave tail which extends to several eddy radii (see Plate 4 in

https://doi.org/10.1017/S0022112098001049 Published online by Cambridge University Press

Swaters 1998). Subsequent to this development the upper layer wave field immediately over the eddy appears more or less steady. The simulation shows that the point of maximum eddy height follows a path which corresponds to a periodic cross-slope oscillation superimposed on an essentially rectilinear along-slope reasonably well described by the Nof velocity (see figure 6 in Swaters 1998).

In a third simulation, Swaters (1998) describes the evolution of a cold dome and upper layer pressure field which initially satisfies the Mory–Stern isolation constraint (2.1). Thus, while the upper layer had a cyclonic eddy located over the cold dome, there was no initial upper layer topographic Rossby wave field. In this simulation one does not see the rapid development of topographic Rossby wave tail (see Plate 2 in Swaters 1998) like in the second simulation just described and one does not see the development of cross-slope oscillations in the path of the point of maximum height of the cold dome.

We speculate that the difference in the propagation characteristics for the point of maximum height of the cold dome observed in the first two simulations compared to the third simulation is a consequence of the suppressed development of the topographic Rossby wave tail in the last simulation due to the fact that the initial eddy–upper layer configuration satisfies the zero topographic Rossby wave condition (2.1). Consequently, there is no significant dynamical interaction in the third simulation between an upper layer topographic Rossby wave field and the lower layer cold dome. It is our contention that the sub-inertial oscillations seen in the Swaters (1998) simulations are the consequence of a dynamical baroclinic interaction between a upper layer topographic Rossby wave field and the lower layer cold dome. It is toward that goal that this paper is directed.

Examining (3.10) and (3.11) one sees that the presence of the second term in (3.10) will lead to azimuthal mode mixing, i.e. the spatial and temporal structure of the amplitudes of the azimuthal modes are coupled. In principle, one can, at least formally, solve the infinite set of coupled equations via a Laplace–Bessel transform technique.

For realistic parameter values, however, the essential and phenomenologically relevant leading-order structure of the solution can be easily determined after exploiting one additional approximation. Assuming that, on average, the coefficients $r^{-1}h_{0_r}$ and $r^{-1}\eta_{0_r}$ are small, then it is possible construct a simple solution which illuminates the leading-order interaction between the eddy and the exterior topographic Rossby wave field.

This approximation is relevant. For example, if we consider an eddy height profile of the form $h_0(r) = h_{0_{max}}\left[1+\cos\left(\pi r/a_0\right)\right]/2$ for $0 \leqslant r \leqslant a_0$ and $h_0(r) = 0$ for $r > a_0$, then the *average* values that $\left|r^{-1}\eta_{0_r}\right|$ and $\left|r^{-1}h_{0_r}\right|$ take on the interval $r \in (0, a_0)$ are about $O\left(10^{-1}\right)$ and $O\left(10^{-2}\right)$, respectively, where we assume $h_{0_{max}}$ is $O(1)$ and a_0 is on the same order as that determined by (2.7), i.e. $a_0 \simeq 6.8$. Other height profiles, e.g., the parabolic profile $h_0(r) = h_{0_{max}}\left[1-\left(r/a_0\right)^2\right]$ for $0 \leqslant r \leqslant a_0$ and $h_0(r) = 0$ for $r > a_0$, give similar results.

This approximation is equivalent to assuming that there is a separation between the length scales associated with the zeroth-order solution for the eddy and the time-dependent anomalies, respectively, which will develop due to interactions with the topographic Rossby wave field. That is, we are making a WKB-like approximation in the solution for (3.10) and (3.11). We will show, *a posteriori*, that this is a reasonable approximation (see e.g. figure 4). The numerical simulation which we describe in § 5 also has this property.

https://doi.org/10.1017/S0022112098001049 Published online by Cambridge University Press

Thus, if we assume that $r^{-1}\eta_{0_r} \simeq O(\varepsilon)$ and $r^{-1}h_{0_r} \simeq O(\varepsilon^2)$, (3.11) suggests that $t \simeq O(\varepsilon^{-1})$ and $h \simeq O(\varepsilon)$ if $\eta \simeq O(1)$, which is suggested by (3.17). To make this formal we introduce the re-scalings

$$\widehat{t} = \varepsilon t, \quad h = \varepsilon \widehat{h}, \quad \eta_{0_r} = \varepsilon \widehat{\eta}_{0_r}, \quad h_{0_r} = \varepsilon^2 \widehat{h}_{0_r}, \tag{3.20}$$

where, to be concrete, we define the parameter ε as the average values that $\left|r^{-1}\eta_{0_r}\right|$ takes over $r \in (0, a_0)$, i.e.,

$$\varepsilon = \frac{1}{a_0}\int_0^{a_0} \left|r^{-1}\eta_{0_r}\right| \, \mathrm{d}r \simeq O\left(10^{-1}\right).$$

It is important to appreciate that with ε defined like this, $\widehat{\eta}_{0_r}$ and $\widehat{h}_{0_r}$ are $O(1)$ quantities.

Substitution of (3.20) into (3.10) and (3.11) gives, after dropping the carets,

$$\varepsilon\Delta\eta_t - \left[\cos(\theta)\,\partial_r - \frac{\sin(\theta)}{r}\partial_\theta\right](\Delta\eta + \eta + \varepsilon h) + \varepsilon\frac{\eta_{0_r}}{r}(\Delta\eta + \eta)_\theta + \varepsilon^2\frac{h_{0_r}}{r}\eta_\theta = 0, \tag{3.21}$$

$$h_t + \frac{\eta_{0_r}}{r}h_\theta - \frac{h_{0_r}}{r}\eta_\theta = 0. \tag{3.22}$$

Assuming a straightforward asymptotic solution to (3.21) and (3.22) of the form

$$(\eta, h) \simeq (\eta, h)^{(0)} + \varepsilon(\eta, h)^{(1)} + O\left(\varepsilon^2\right),$$

leads to the $O(1)$ and $O(\varepsilon)$ problems, respectively,

$$\Delta\eta^{(0)} + \eta^{(0)} = 0, \tag{3.23}$$

$$h_t^{(0)} + \frac{\eta_{0_r}}{r}h_\theta^{(0)} = \frac{h_{0_r}}{r}\eta_\theta^{(0)}, \tag{3.24}$$

$$\Delta\eta^{(1)} + \eta^{(1)} = -h^{(0)}, \tag{3.25}$$

where we have not included the $O(\varepsilon)$ problem associated with (3.22). The initial condition for $\eta^{(0)}$ is (3.17) and the initial conditions for $\eta^{(1)}$ and $h^{(0)}$ are that $\eta^{(1)} = h^{(0)} = 0$ at $t = 0$.

The solution to (3.23) subject to (3.17) is simply (3.17) itself, i.e.

$$\eta^{(0)}(r, \theta, t) = \frac{4}{\pi}\sum_{n=0}^{\infty}\frac{J_{2n+1}(r)\cos[(2n+1)\theta]}{2n+1}, \tag{3.26}$$

which when substituted into (3.24), gives a solution for $h^{(0)}$, which satisfies (3.18), in the form

$$h^{(0)}(r, \theta, t) = \frac{4h_{0_r}(r)}{\pi\eta_{0_r}(r)}\sum_{n=0}^{\infty}\frac{J_{2n+1}(r)}{2n+1} \times\left\{\cos[(2n+1)\theta] - \cos\left[(2n+1)\left(\theta - \frac{\eta_{0_r}(r)}{r}t\right)\right]\right\}. \tag{3.27}$$

As discussed more completely in the next section, the time evolution of $h^{(0)}(r, \theta, t)$ corresponds to a superposition of azimuthally travelling waves with a radially dependent phase speed. As time increases, this geometrical dispersion develops into spiral-like perturbations on the eddy boundary. In addition, we note that the sum

https://doi.org/10.1017/S0022112098001049 Published online by Cambridge University Press

$\eta_0(r) + \mu\eta^{(0)}(r,\theta,t)$, i.e. (3.15) + μ(3.26), will satisfy the radiation condition (2.4) for all $t \geqslant 0$.

With $h^{(0)}(r,\theta,t)$ determined by (3.27), a particular solution for $\eta^{(1)}(r,\theta,t)$, as determined by (3.25) and denoted as $\eta_p^{(1)}(r,\theta,t)$, can be written in the form

$$\eta_p^{(1)} = \sum_{n=0}^{\infty} F_{2n+1}(r,t)\sin[(2n+1)\theta] + H_{2n+1}(r,t)\cos[(2n+1)\theta], \tag{3.28}$$

where

$$F_{2n+1} = \frac{2Y_{2n+1}(r)}{2n+1}\int_0^r \frac{\xi J_{2n+1}^2(\xi)\,h_{0_\xi}(\xi)}{\eta_{0_\xi}(\xi)}\sin\left[(2n+1)\,\eta_{0_\xi}(\xi)\,t/\xi\right]\mathrm{d}\xi$$
$$+\frac{2J_{2n+1}(r)}{2n+1}\int_r^{a_0} \frac{\xi J_{2n+1}(\xi)\,Y_{2n+1}(\xi)\,h_{0_\xi}(\xi)}{\eta_{0_\xi}(\xi)}\sin\left[(2n+1)\,\eta_{0_\xi}(\xi)\,t/\xi\right]\mathrm{d}\xi, \tag{3.29}$$

$$H_{2n+1} = \frac{2Y_{2n+1}(r)}{2n+1}\int_0^r \frac{\xi J_{2n+1}^2(\xi)\,h_{0_\xi}(\xi)}{\eta_{0_\xi}(\xi)}\left\{\cos\left[(2n+1)\,\eta_{0_\xi}(\xi)\,t/\xi\right]-1\right\}\mathrm{d}\xi$$
$$+\frac{2J_{2n+1}(r)}{2n+1}\int_r^{a_0} \frac{\xi J_{2n+1}(\xi)\,Y_{2n+1}(\xi)\,h_{0_\xi}(\xi)}{\eta_{0_\xi}(\xi)}\left\{\cos\left[(2n+1)\,\eta_{0_\xi}(\xi)\,t/\xi\right]-1\right\}\mathrm{d}\xi. \tag{3.30}$$

While this particular solution satisfies the appropriate initial condition, i.e. $\eta^{(1)}(r,\theta,0) = 0$, it does not satisfy the radiation condition (2.4) since

$$F_{2n+1}(r,t) = \Gamma_{2n+1}(t)\,Y_{2n+1}(r), \tag{3.31}$$

$$H_{2n+1}(r,t) = \Phi_{2n+1}(t)\,Y_{2n+1}(r), \tag{3.32}$$

for $r \geqslant a_0$, where

$$\Gamma_{2n+1} = \frac{2}{2n+1}\int_0^{a_0} \frac{\xi J_{2n+1}^2(\xi)\,h_{0_\xi}(\xi)}{\eta_{0_\xi}(\xi)}\sin\left[(2n+1)\,\eta_{0_\xi}(\xi)\,t/\xi\right]\mathrm{d}\xi, \tag{3.33}$$

$$\Phi_{2n+1} = \frac{2}{2n+1}\int_0^{a_0} \frac{\xi J_{2n+1}^2(\xi)\,h_{0_\xi}(\xi)}{\eta_{0_\xi}(\xi)}\left\{\cos\left[(2n+1)\,\eta_{0_\xi}(\xi)\,t/\xi\right]-1\right\}\mathrm{d}\xi, \tag{3.34}$$

so that $\eta_p^{(1)}(r,\theta,t) \simeq O\left(r^{-1/2}\right)$ as $r \to \infty$.

In order to satisfy the radiation condition (2.4) we must add a homogeneous solution, denoted as $\eta_h^{(1)}(r,\theta,t)$, to (3.25), in the form

$$\eta_h^{(1)} = \sum_{n=0}^{\infty}\sum_{m=0}^{\infty}\left[A_{2n+1,2m}(t)\sin(2m\theta) + B_{2n+1,2m}(t)\cos(2m\theta)\right]J_{2m}(r), \tag{3.35}$$

see e.g. Miles (1968) or Swaters & Flierl (1991), since the even $J_m(r)$ functions have the same asymptotic form as the odd $Y_n(r)$ functions as $r \to \infty$.

Comparing the parity of the trigonometric terms implies that the $A_{2n+1,2m}$ and $B_{2n+1,2m}$ coefficients must satisfy the constraints

$$\Gamma_{2n+1}(t)\sin[(2n+1)\theta] = \sum_{m=1}^{\infty}(-1)^{n+m}A_{2n+1,2m}(t)\sin(2m\theta), \tag{3.36}$$

$$\Phi_{2n+1}(t)\cos[(2n+1)\theta] = \sum_{m=0}^{\infty}(-1)^{n+m}B_{2n+1,2m}(t)\cos(2m\theta), \tag{3.37}$$

https://doi.org/10.1017/S0022112098001049 Published online by Cambridge University Press

in the sector $|\theta| < \pi/2$, which implies

$$A_{2n+1,2m} = \frac{8m\Gamma_{2n+1}}{\pi\left[(2n+1)^2 - 4m^2\right]}, \tag{3.38}$$

$$B_{2n+1,2m} = \frac{(4-2\delta_{0m})(2n+1)\,\Phi_{2n+1}}{\pi\left[(2n+1)^2 - 4m^2\right]}. \tag{3.39}$$

If one examines the structure of the expressions for $h^{(0)}$, $\eta^{(0)}$ and $\eta^{(1)}$ one sees that re-writing these expressions in terms of the uncareted variables in (3.20) leaves the expressions unchanged, i.e. the ε coefficients all cancel out. Thus, in summary, we have determined an approximate solution to (3.3) and (3.4) in the form

$$h \simeq h_0(r) + \mu h^{(0)}(r,\theta,t) + O\left[\mu\left(\frac{h_{0_r}}{\eta_{0_r}}\right)^2, \mu^2\right], \tag{3.40}$$

$$\eta \simeq \eta_0(r) + \mu\left\{\eta^{(0)}(r,\theta) + \eta^{(1)}(r,\theta,t)\right\} + O\left[\mu\left(\frac{h_{0_r}}{\eta_{0_r}}\right)^2, \mu^2\right], \tag{3.41}$$

where η_0, $\eta^{(0)}$ and $h^{(0)}$ are given by (3.15), (3.26) and (3.27), respectively, and where it is convenient to write $\eta^{(1)}$ in the form

$$\eta^{(1)} = \sum_{n=0}^{\infty} F_{2n+1}\sin\left[(2n+1)\theta\right] + H_{2n+1}\cos\left[(2n+1)\theta\right] + \Psi_{2n+1}, \tag{3.42}$$

with

$$\Psi_{2n+1} = \sum_{m=0}^{\infty}\left[A_{2n+1,2m}\sin(2m\theta) + B_{2n+1,2m}\cos(2m\theta)\right]J_{2m}(r), \tag{3.43}$$

where F_{2n+1}, H_{2n+1}, $A_{2n+1,2m}$ and $B_{2n+1,2m}$ are given by (3.29), (3.30), (3.38) and (3.39), respectively, and where all these expressions are, and henceforth are assumed to be, evaluated in terms of the uncareted variables associated with (3.20). Again, we emphasize that (3.41) is uniformly valid over $(x,y) \in \mathbb{R}^2$ and satisfies the radiation condition (2.4) and that both (3.40) and (3.41) satisfy the initial conditions (3.17) and (3.18).

With the above solutions we can determine the deformation to the eddy boundary or incropping. Assuming that we can evaluate (3.14) by taking the limit as $r \uparrow a_0$, it follows that

$$a(\theta,t) = -\lim_{r\uparrow a_0}\frac{h(r,\theta,t)}{h_{0_r}(r)},$$

which, if (3.27) is substituted in, implies

$$a(\theta,t) \simeq \frac{4}{\pi\eta_{0_r}(a_0)}\sum_{n=0}^{\infty}\frac{J_{2n+1}(a_0)}{2n+1} \times\left\{\cos\left[(2n+1)\left(\theta - \frac{\eta_{0_r}(a_0)}{a_0}t\right)\right] - \cos\left[(2n+1)\theta\right]\right\}. \tag{3.44}$$

It follows from (3.15) that $\mu \neq 0 \Longrightarrow \eta_{0_r}(a_0) \neq 0$ (except if $Y_1(a_0) = 0$) so that, in general, this expression is well defined. Note that (3.44) will satisfy the initial condition (3.19).

https://doi.org/10.1017/S0022112098001049 Published online by Cambridge University Press

4. Discussion

Given that we have derived approximate, but nevertheless uniformly valid, solutions for the time evolution of the eddy height and the topographic Rossby wave field, we are now in a position to compute the right-hand side of the centre of mass equations (3.5) and (3.6). If (3.40) and (3.41) are substituted into (3.5) and (3.6), we may write the resulting expressions in the form

$$\begin{aligned}\partial_t X_{mass}(t) &\simeq -\frac{\mu \int\int_{\Omega} h_0 \left[\eta^{(0)} + \eta^{(1)}\right]_y + h^{(0)}\eta_{0_y}\,\mathrm{d}x\mathrm{d}y}{2\pi \int_0^{a_0} r h_0(r)\,\mathrm{d}r} \\ &= -\frac{\mu \int_0^{2\pi}\int_0^{a_0} r\sin(\theta)\left[h^{(0)}\eta_{0_r} - \left(\eta^{(0)} + \eta^{(1)}\right)h_{0_r}\right]\mathrm{d}r\mathrm{d}\theta}{2\pi \int_0^{a_0} r h_0(r)\,\mathrm{d}r} \\ &= \frac{\mu \int_0^{a_0} r\left\{4J_1(r)\,h_{0_r}(r)\sin\left[\eta_{0_r}(r)\,t/r\right] + \pi F_1(r,t)\,h_{0_r}(r)\right\}\mathrm{d}r}{2\pi \int_0^{a_0} r h_0(r)\,\mathrm{d}r},\end{aligned} \tag{4.1}$$

where we have integrated by parts once using $h_0(a_0) = 0$ and exploited the orthogonality of the trigonometric functions after directly substituting in the solutions for $\eta^{(0)}$, $\eta^{(1)}$ and $h^{(0)}$.

Similarly, it follows that

$$\partial_t Y_{mass}(t) \simeq -\frac{\mu \int_0^{a_0} r\left\{4J_1(r)\,h_{0_r}(r)\cos\left[\eta_{0_r}(r)\,t/r\right] + \pi H_1(r,t)\,h_{0_r}(r)\right\}\mathrm{d}r}{2\pi \int_0^{a_0} r h_0(r)\,\mathrm{d}r}. \tag{4.2}$$

Careful examination of the integrals in the numerators of (4.1) and (4.2) shows, however, that

$$\partial_t X_{mass}(t) \simeq 0, \tag{4.3}$$

and

$$\partial_t Y_{mass}(t) \simeq \frac{4\mu^2}{\pi^2 \int_0^{a_0} r h_0(r)\,\mathrm{d}r} > 0, \tag{4.4}$$

to this level of approximation, i.e. in geostationary coordinates, the along-slope position of the centre of mass is well described by the position predicted by the Nof velocity and the down-slope position of the centre of mass increases linearly with respect to time.

To see this, all that is required is to show that those terms in the integrands in the numerator which explicitly contain a time dependence collectively integrate to zero. Let us consider the term in (4.1) which contains the $F_1(r,t)$ factor. This term can be

https://doi.org/10.1017/S0022112098001049 Published online by Cambridge University Press

written in the form

$$\begin{aligned}
&\pi \int_0^{a_0} rF_1(r,t)\, h_{0_r}(r)\, \mathrm{d}r \\
&\quad = 2\pi \int_0^{a_0} rY_1(r)\, h_{0_r}(r) \int_0^r \frac{\xi J_1^2(\xi)\, h_{0_\xi}(\xi)}{\eta_{0_\xi}(\xi)} \sin\left[\eta_{0_\xi}(\xi)\, t/\xi\right] \mathrm{d}\xi \mathrm{d}r \\
&\qquad + 2\pi \int_0^{a_0} rJ_1(r)\, h_{0_r}(r) \int_0^r \frac{\xi J_1(\xi)\, Y_1(\xi)\, h_{0_\xi}(\xi)}{\eta_{0_\xi}(\xi)} \sin\left[\eta_{0_\xi}(\xi)\, t/\xi\right] \mathrm{d}\xi \mathrm{d}r \\
&\quad = 2\pi \int_0^{a_0} \frac{\xi J_1(\xi)\, h_{0_\xi}(\xi)}{\eta_{0_\xi}(\xi)} \sin\left[\eta_{0_\xi}(\xi)\, t/\xi\right] \\
&\qquad \times \left\{ Y_1(\xi) \int_0^{\xi} rJ_1(r)\, h_{0_r}(r)\, \mathrm{d}r + J_1(\xi) \int_{\xi}^{a_0} rJ_1(r)\, h_{0_r}(r)\, \mathrm{d}r \right\} \mathrm{d}\xi \\
&\quad = -4 \int_0^{a_0} \xi J_1(\xi)\, h_{0_\xi}(\xi) \sin\left[\eta_{0_\xi}(\xi)\, t/\xi\right], \qquad (4.5)
\end{aligned}$$

where we have substituted in (3.29) evaluated for $n = 0$, interchanged the order of the integration and used the Green's function representation for η_{0_r} based on (3.15). Clearly, (4.5) is the negative of the first term in the numerator of (4.1) so that (4.3) follows.

Similarly, all those terms in the numerator in (4.2) which have an explicit time dependence in them collectively integrate to zero so that (4.2) exactly reduces to

$$\begin{aligned}
\partial_t Y_{mass} &\simeq -\frac{2\mu \displaystyle\int_0^{a_0} rJ_1(r)\, h_{0_r}(r)\, \mathrm{d}r}{\pi \displaystyle\int_0^{a_0} rh_0(r)\, \mathrm{d}r} \\
&= \frac{2\mu \displaystyle\int_0^{a_0} rJ_0(r)\, h_0(r)\, \mathrm{d}r}{\pi \displaystyle\int_0^{a_0} rh_0(r)\, \mathrm{d}r} = \frac{4\mu^2}{\pi^2 \displaystyle\int_0^{a_0} rh_0(r)\, \mathrm{d}r},
\end{aligned}$$

implying, to this level of approximation, that

$$Y_{mass}(t) \simeq \frac{4\mu^2 t}{\pi^2 \displaystyle\int_0^{a_0} rh_0(r)\, \mathrm{d}r}. \qquad (4.6)$$

In the next section we will present a numerical simulation which qualitatively confirms our leading-order predictions for $X_{mass}(t)$ and $Y_{mass}(t)$.

It is important to appreciate that the down-slope motion arises in a completely analogous manner to the southward motion calculated by Flierl (1984) for a radiating warm ring on a β-plane. The wave field, which radiates energy into the far field, exerts a wave drag on the cold dome. The motion associated with this drag is in geostrophic balance which results in the cold dome being deflected in the down-slope direction (down slope is, of course, the same as 'southward' thinking of the sloping bottom as a topographic β-plane). Alternatively, one can view the energy source for the upper layer wave field as the potential energy associated with the cold dome. As the cold dome slides down the slope, it releases potential energy which is radiated away as topographic Rossby waves.

The magnitude of the down-slope speed of the centre of mass is a function of

https://doi.org/10.1017/S0022112098001049 Published online by Cambridge University Press

both the maximum height and the radius of the initial eddy configuration. If (3.16) is substituted into (4.4), it follows that

$$\partial_t Y_{mass} \simeq \frac{\left[\int_0^{a_0} rJ_0(r)\, h_0(r)\ \mathrm{d}r\right]^2}{\int_0^{a_0} rh_0(r)\ \mathrm{d}r}. \tag{4.7}$$

If we denote the maximum height of the eddy at $t = 0$ as $h_{0_{max}}$, (4.7) suggests that

$$\partial_t Y_{mass}(t) \propto h_{0_{max}}. \tag{4.8}$$

The dependence of the down-slope speed of the centre of mass on the initial eddy radius is not monotonic. For the purposes of this discussion it is useful to denote the right-hand side of (4.7) as $\mathscr{F}(a_0)$, i.e.

$$\mathscr{F}(a_0) \equiv \frac{\left[\int_0^{a_0} rJ_0(r)\, h_0(r)\ \mathrm{d}r\right]^2}{\int_0^{a_0} rh_0(r)\ \mathrm{d}r}. \tag{4.9}$$

If we denote the (first non-zero) value of a_0 for which $\mu = 0$ by a_*, it follows from (4.9) that $\mathscr{F}(0) = \mathscr{F}(a_*) = 0$ and $\mathscr{F}(a_0) > 0$ for $a_0 \in (0, a_*)$. Thus $\mathscr{F}(a_0)$ will be maximized for some interior value of the interval $(0, a_*)$. The precise value of the maximizer and the maximum value of $\mathscr{F}(a_0)$ will depend on the shape of $h_0(r)$.

As an example, consider the smooth initial eddy profile

$$h_0(r) = \frac{h_{0_{max}}}{2}\left[1 + \cos\left(\frac{\pi r}{a_0}\right)\right], \tag{4.10}$$

for $r \leqslant a_0$ and zero elsewhere. It follows that

$$\partial_t Y_{mass} \simeq \mathscr{F}(a_0) = \frac{4\pi^2 h_{0_{max}}\left\{\int_0^{a_0} rJ_0(r)\left[1 + \cos\left(\frac{\pi r}{a_0}\right)\right]\mathrm{d}r\right\}^2}{a_0^2(\pi^2 - 4)}, \tag{4.11}$$

and $a_* \simeq 6.85$.

In figure 2 we plot $\mathscr{F}(a_0)$ for $a_0 \in [0, a_*]$ for $h_{0_{max}} = 1.0$. One can see the behaviour just described. The maximum cross-slope velocity occurs at $a_0 \simeq 2.58$ with magnitude approximately 0.45. Based on the scalings relevant for the observations of Houghton *et al.* (1982), the maximum cross-slope velocity would be about 2 cm/s for a cold pool with radius about 30 km and maximum height about 35 m, and for the Strait of Georgia observations (LeBlond *et al.* 1991; Karsten *et al.* 1995), the cross-slope velocity would be about 8 cm s^{-1} for a cold pool with radius about 18 km and maximum height about 60 m.

Even though the trajectory followed by the centre of mass is essentially rectilinear, the evolution of the eddy height and overlying topographic Rossby wave field is not steady. We now turn to describing these characteristics associated with an initial eddy height profile given by (4.10). In order to introduce a sufficiently large perturbation so that we can effectively illustrate the spatial structure and temporal characteristics of the dynamical interaction we choose $a_0 = 0.9a_* \simeq 6.17$ and $h_{0_{max}} = 1.0$. This implies that $\mu \simeq 0.36$ and that the average values that $r^{-1}\eta_{0_r}$ and $r^{-1}h_{0_r}$ and take on the

https://doi.org/10.1017/S0022112098001049 Published online by Cambridge University Press

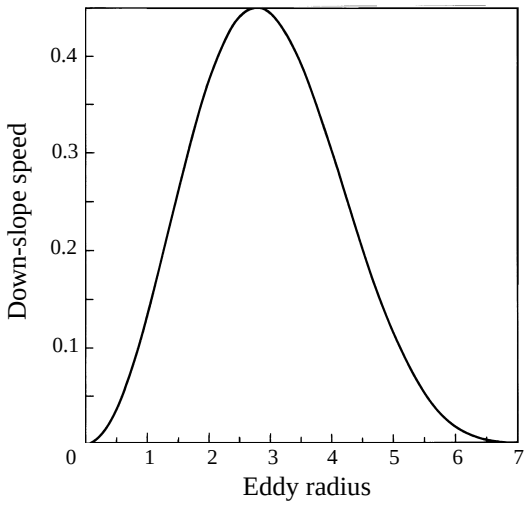


FIGURE 2. Down-slope velocity of the centre of mass, i.e. $\partial_t Y_{mass}$, as a function of the initial eddy radius a_0 for the smooth initial eddy height profile (4.10) with $h_{0_{max}} = 1.0$.

interval $(0, a_0)$ are approximately 0.2 and 0.07, respectively. The cross-slope velocity associated with the centre of mass is given by $\partial_t Y_{mass}(t) \simeq 0.01$.

One of the major motivations for this paper is our attempt to develop a simple model for the oscillations observed in the position of maximum height of the eddy generated in the coupled density front instability simulation reported by Swaters (1998). We can interpret these oscillations as a consequence of the structure of the time evolution of the height field $h^{(0)}(r, \theta, t)$ given by (3.27). The time evolution of $h^{(0)}(r, \theta, t)$ corresponds to a superposition of azimuthally travelling waves with a radially dependent phase speed. These anomalies result in the coordinates of the maximum total height of the eddy, i.e. $h_0 + \mu h^{(0)}$, not being located at and, in fact, precessing about $r = 0$ (relative to the Nof frame of reference). This leads to the position and magnitude of maximum height oscillating in time.

In figure 3(a, b) we show the along- and cross-slope coordinates of the maximum total height of the eddy as a function of time relative to the Nof frame of reference, denoted as $(X_{max}(t), Y_{max}(t))$, which are determined implicitly from

$$\nabla \left[h_0 + \mu h^{(0)}\right](X_{max}(t), Y_{max}(t), t) = \mathbf{0}. \tag{4.12}$$

One can clearly see the oscillations in the coordinates. In figure 3(c, d) we show the along-slope coordinate of the position of maximum height in the geostationary fame, i.e. $X_{max}(t) + t$, and the magnitude of the maximum height versus time, respectively.

The magnitude and period of the oscillations is dependent on the values of a_0 and $h_{0_{max}}$. Increasing (decreasing) $h_{0_{max}}$ leads to increasing (decreasing) the frequency and amplitude of the oscillations. Increasing (decreasing) a_0 near a_* (which forms the basis for the underlying weakly radiating asymptotic approximation) leads to decreasing (increasing) the frequency and amplitude of the oscillations. In addition, one can see that $X_{max}(t)$ and $Y_{max}(t)$ are 90° out of phase. The numerical simulation we present in the next section will exhibit these oscillations.

In figures 4 and 5 we present grey-scale plots in the Nof frame of reference of the total eddy height and upper layer geostrophic pressure

$$\eta \simeq \eta_0(r) + \mu \left\{\eta^{(0)}(r, \theta) + \eta^{(1)}(r, \theta, t)\right\},$$

https://doi.org/10.1017/S0022112098001049 Published online by Cambridge University Press

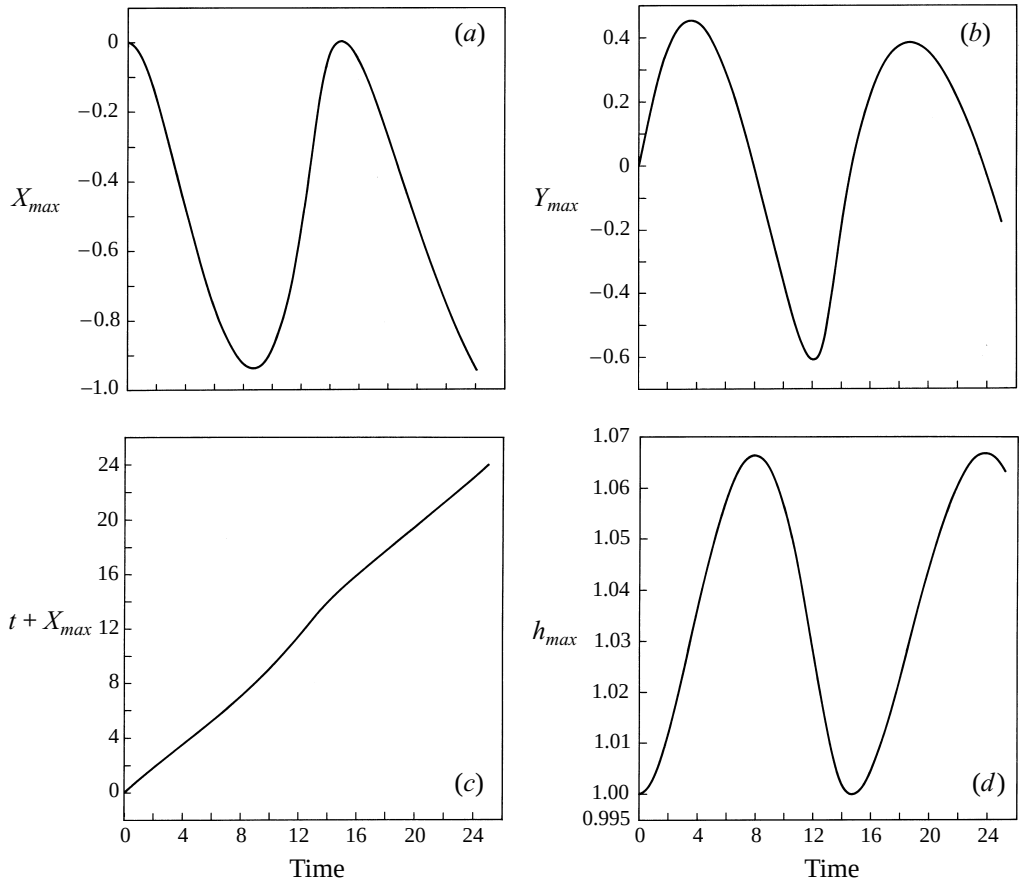


FIGURE 3. (*a*, *b*) The along-slope and cross-slope positions of the maximum total eddy height, relative to the Nof frame of reference, versus time, respectively, as determined by (4.12) for the smooth initial eddy height profile (4.10) with $h_{0max} = 1.0$ and $a_0 = 0.9a_*$. (*c*) The along-slope position of the maximum height in geostationary coordinates versus time. (*d*) The value of the maximum height versus time.

at $t = 0$, 8.33, 16.66 and 25.0, associated with the initial eddy height profile (4.10) with $a_0 = 0.9a_*$ and $h_{0_{\max}} = 1.0$. The gray scale is shown at the bottom of the figures. In figure 4, the grey-scale is linear with white corresponding to 0.0 and black corresponding to values $\gtrsim 1.0$.

Since we are more interested in the pattern formed for the upper layer topographic wave field rather than in the precise numerical values, it was more convenient to use a variable grey scale in figure 5. In each frame, the grey scale linearly spans the range between the individual minimum and maximum values with black corresponding to the minimum and white corresponding to the maximum values. Note that the grey scale used for the eddy height is 'inverted' compared to that used for the upper layer stream function, i.e. white through to black corresponds to increasing values in figure 4, whereas it corresponds to decreasing values in figure 5. We found this arrangement somewhat more visually satisfying.

The coordinates are arranged so that left to right in each panel corresponds to the direction of increasing x, i.e. the along-slope direction, and the bottom to top direction in each panel corresponds to increasing y, i.e. the down-slope direction. The

https://doi.org/10.1017/S0022112098001049 Published online by Cambridge University Press

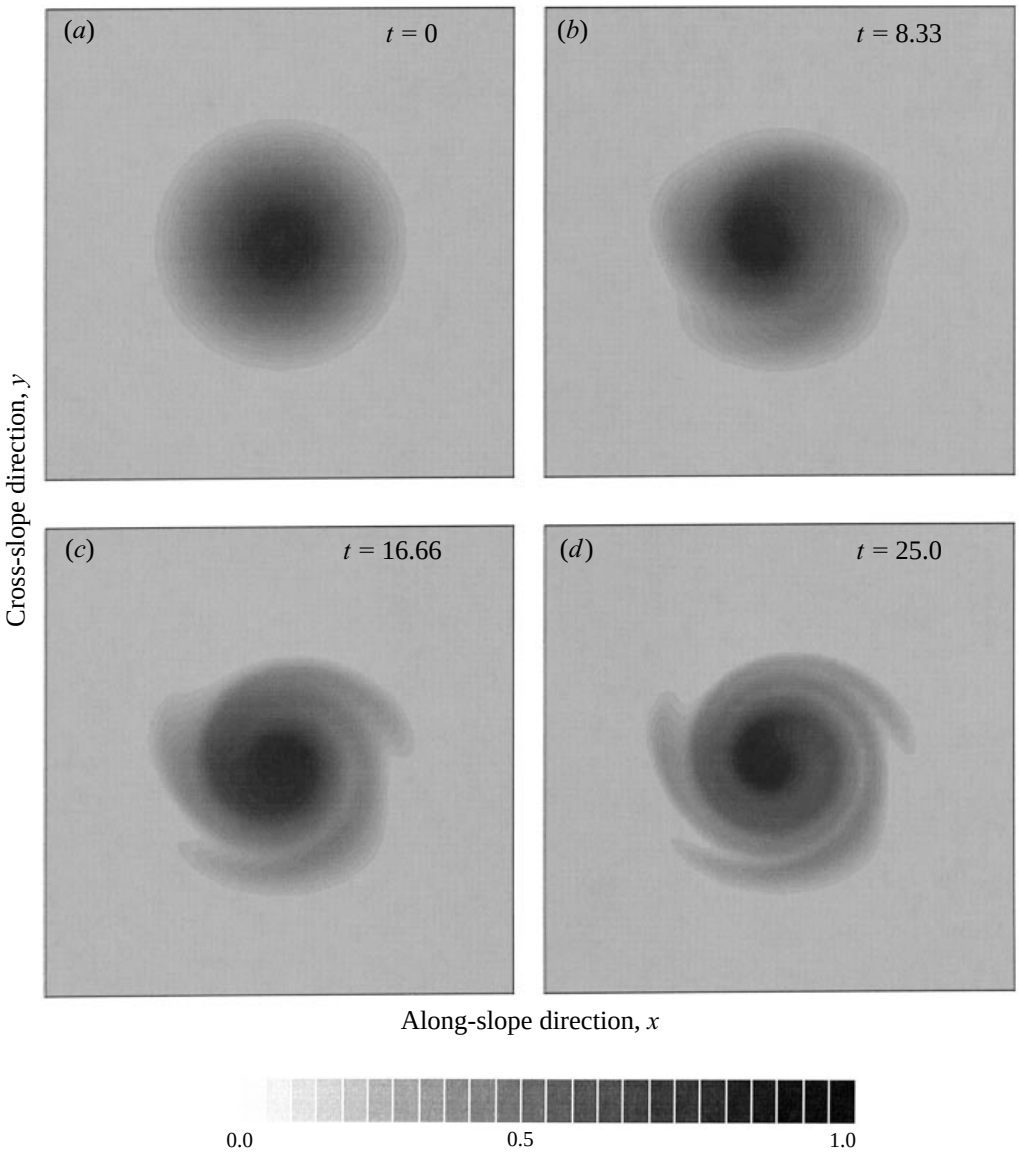


FIGURE 4. Sequence of horizontal grey-scale plots for the total eddy height as determined by (4.12) for the initial eddy height profile described in figure 3 for $t = 0.0$, 8.33, 16.66 and 25.0, respectively.

coordinate span in each panel in figures 4 and 5 corresponds to $-10 \leqslant x, y \leqslant 10$ and $-20 \leqslant x, y \leqslant 20$, respectively, in the co-moving frame. We chose these ranges of (x, y) values in order to effectively illustrate the evolution of the lower layer eddy height and upper layer wave fields, respectively.

In figure 4(a) the lower layer height at $t = 0$ is shown and is, of course, exactly radially symmetric. The corresponding upper layer pressure field is shown in figure 5(a). The more or less circular black region corresponds to the cyclonic eddy region associated with (3.15). One can see the crescent shaped contours 'behind' the eddy corresponding to the topographic Rossby wave field. Ahead of the eddy region, the upper layer pressure field rapidly vanishes as a result of the radiation condition. The

https://doi.org/10.1017/S0022112098001049 Published online by Cambridge University Press

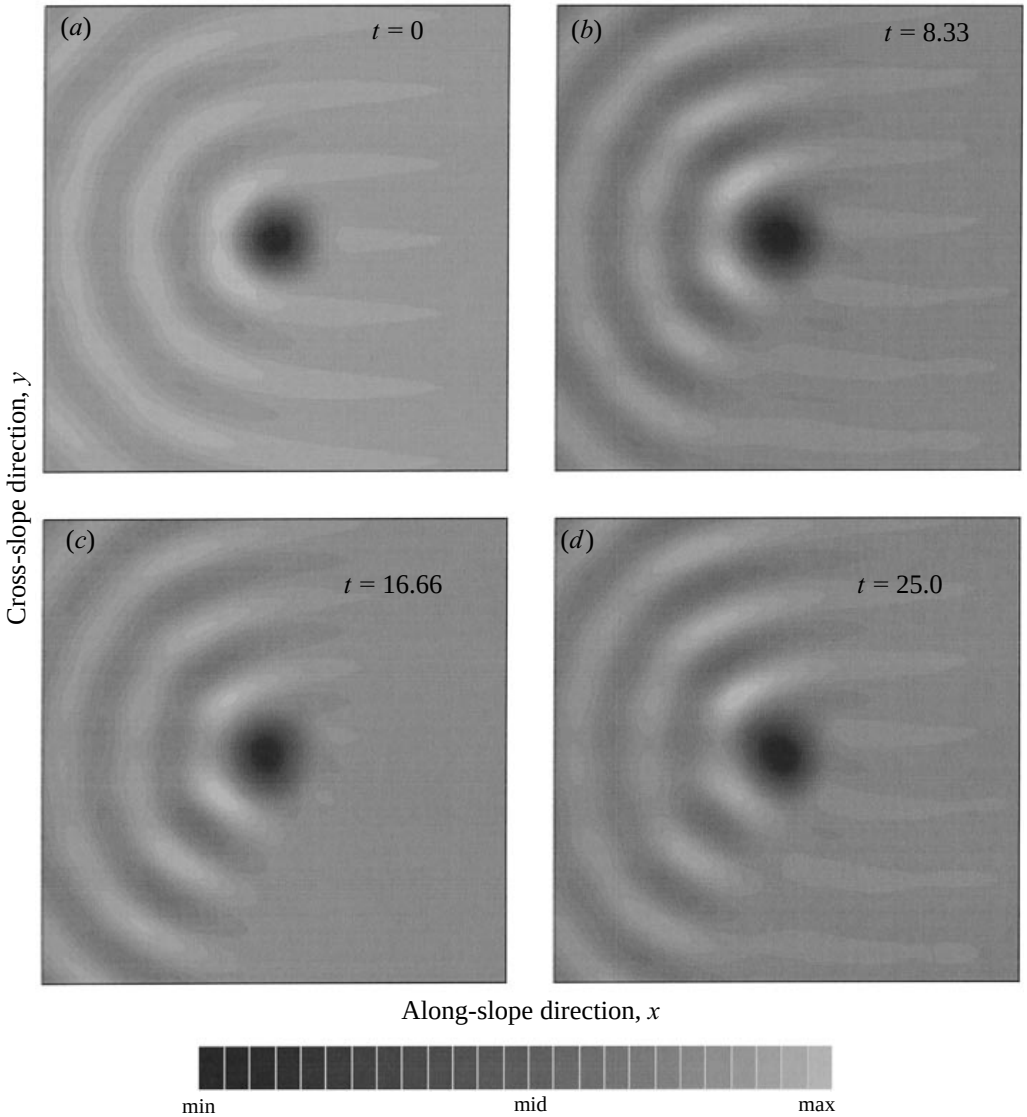


FIGURE 5. Sequence of horizontal grey-scale plots for the total upper layer geostrophic pressure $\eta_0(r) + \mu\left\{\eta^{(0)}(r,\theta) + \eta^{(1)}(r,\theta,t)\right\}$ for the initial eddy height profile described in figure 3 and same times as figure 4.

shape of the initial wave field shown in figure 5(*a*) is identical to that calculated by Flierl (1984; see his figure 4) for a radiating warm-core ring modulo a 180° rotation in orientation due to the fact that the background vorticity gradient points in the negative y-direction (since the mean depth of the upper layer increases in the positive y-direction) in our study in contrast to the geometry found for the usual zonal Cartesian coordinates chosen in β-plane dynamics.

One can see the developing eddy height over time in figure 4(*b–d*). On the eddy boundary, spiral-like perturbations begin to develop and amplify over time into distinct boundary filaments. In addition, in the inner core of the eddy, corresponding to the black region, one can see the loss of radial symmetry as well. The maximum

https://doi.org/10.1017/S0022112098001049 Published online by Cambridge University Press

in the eddy height is located, to a first approximation, in the centre of the darkest region. One can see that this point precesses about the centre coordinates associated with figure 4(*a*). Note that the width of the eddy is large compared to the width of the developing spiral anomalies. This provides justification for the scalings (3.20) which exploits the underlying scale separation between the eddy and (initially at least) developing anomalies.

In this highly idealized inviscid (and essentially quasi-linear) calculation, the spiral anomalies continue to propagate azimuthally as time increases yet further and the eddy develops a complicated banded structure. It is not unreasonable to speculate that this structure would become increasingly unstable and/or other processes such as entrainment, friction or nonlinearity would become important and the banded structure might loose its irregular appearance. We will see this occurring in the fully nonlinear numerical simulation described in the next section.

The corresponding evolution in the structure in the upper layer pressure field is shown in figure 5(*b–d*). We can see that while there remains a distinct central core of cyclonic circulation, there is a time development to the topographic Rossby wave field. There is an observable periodicity over time in the structure of the wave field even ahead of the eddy. Notice how the wave field ahead of the eddy appears to almost vanish in the $t = 16.66$ frame in as much as the crescent shaped contours do not seem to extend into this region. This is, however, only an illusion fostered by the contouring intervals. The structure of the wave field is, in fact, similar to that illustrated in the $t = 8.33$ and 25.0 panels. The dominant crescent shaped pattern behind the eddy remains essentially intact. It even appears to remain largely even about the x-axis even though there are odd contributions in (3.42).

5. Numerical simulation

In this section we present a nonlinear numerical simulation of the governing equations assuming an initial condition corresponding to a weakly radiating cold dome. As we shall see, the numerical simulation has many features which closely resemble the principal predictions of our analytical work. The numerical scheme is essentially identical to that described in Swaters (1998).

Equations (1.1) and (1.2) were numerically solved as the system

$$q_t + J(\eta, q + h_B) = 0, \tag{5.1}$$

$$h_t + J(\eta + h_B, h) = \nu \Delta h, \tag{5.2}$$

$$\Delta\eta = q - h, \tag{5.3}$$

where (5.1), which is the potential vorticity equation for the upper layer, is simply (1.1)+(1.2). Equations (5.1) and (5.2) were integrated forward in time using a 128×128 grid point second-order leapfrog procedure with the Arakawa (1966) finite difference scheme implemented for the Jacobian. A *Robert* filter (Asselin 1972) with coefficient 0.005 was applied at each time step to suppress the computational mode. The upper layer geostrophic pressure η was obtained from (5.3) at each time step using a direct solver. The numerical friction term Δh with coefficient $\nu = 10^{-3}$ was included in (5.2) to suppress relatively high-wavenumber features in the simulations. The equations were solved in the periodic channel

$$\Omega_{num} = \{(x, y) \mid |x| < 30, |y| < 30\}, \tag{5.4}$$

where the periodicity is in the x-direction and we impose $\eta = 0$ on $y = \pm 30$. The

https://doi.org/10.1017/S0022112098001049 Published online by Cambridge University Press

bottom topography is given by

$$h_B = -(y + 30), \tag{5.5}$$

so that the Nof velocity is simply given by $\boldsymbol{e}_1$.

We did a number of simulations before deciding on the domain size. Our goal was to have a computational domain small enough that the cold dome and any subsequent anomalies which might form would be adequately resolved. At the same time, the computational domain had to be large enough so that we could adequately model the topographic Rossby wave tail. The above computational domain satisfied these requirements. Our simulation had about 26 grid points along a radial cross-section within the cold dome and thus in that part of the upper layer wave field immediately over the cold dome.

The periodic boundary conditions in the x-direction allow upper layer wave energy to radiate out of the domain in the along-slope direction. However, in order to suppress wave energy from re-entering the domain along the $x = 30$ boundary, we imposed a sponge layer in the immediate neighbourhood of $x = \pm 30$ with a spatially varying damping coefficient. The cross-slope boundaries, i.e. $y = \pm 30$, were far enough away from the trajectory of the cold dome that imposing homogeneous Dirichlet boundary conditions on η on $y = \pm 30$ did not dramatically affect our results.

The initial condition is shown in figure 6. For the upper layer stream function or geostrophic pressure, the initial condition is given by (2.8) and (2.9). Although the initial wave field had a relatively small amplitude near the cross-slope computational boundaries, we applied a tapered filter near $y = \pm 30$ to smoothly satisfy the boundary conditions. For the initial cold dome height, we assume the profile (4.10) with $h_{0_{max}} = 1.0$ and $a_0 = 0.9a_* \simeq 6.17$ (implying $\mu \simeq 0.36$). This is the same initial condition as that used to generate figures 3, 4 and 5. However, for the numerical simulation, the initial cold dome is centred at coordinates $(-10.0, 0)$. We remark that since $h(x, y, 0)$ is continuously differentiable, it follows from (2.8) and (2.9) that $\eta(x, y, 0)$ is, in fact, three-times continuously differentiable. This means that the initialized Jacobian terms in (5.1) and (5.2) are continuous at the cold dome boundary $r = a_0$. Again, we point out that the shape of the initial topographic Rossby wave field shown in figure 6 (and later in figure 8) is identical to that determined by Flierl (1984; see his figure 4).

The entire computational domain is shown in figure 6. The orientation of the panels is the same as in figures 4 and 5 with left to right and bottom to top corresponding to increasing x and y values, respectively. Note that the upper layer stream function satisfies, of course, the no upstream waves condition.

In figure 7 we present a sequence of grey-scale plots of the cold dome height. In order to facilitate comparison with the theoretical work, the plots are in the Nof frame of reference and have the same horizontal domains, times and grey scale as in figure 4. The coordinate range in each panel in figure 7 corresponds to $-20+t \leqslant x \leqslant t$ and $-10 \leqslant y \leqslant 10$, respectively, i.e. we are showing a translating sub-domain of the computational domain in each panel.

The similarity between figures 4 and 7 is striking. The $t = 0$ panels are, of course, identical. As time evolves we see the development of the spiral anomalies. The $t = 8.33$ panels are very similar with what appears to be three similarly placed spiral anomalies developing. However, in the $t = 16.66$ and 25.0 panels, the numerical simulation seems to be dominated by a two-spiral structure whereas the theoretical solution retains a three-spiral structure. It is interesting to note though that the two spiral arms located

https://doi.org/10.1017/S0022112098001049 Published online by Cambridge University Press

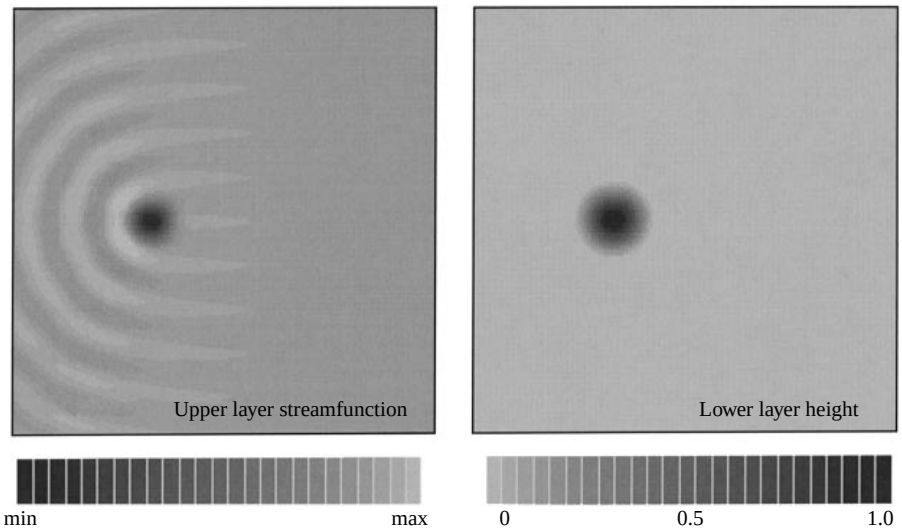


FIGURE 6. Initial condition assumed for the upper layer geostrophic pressure and lower layer cold dome height for the numerical simulation.

on the down- and up-slope sides in the theoretical solution are positioned in a very similar manner to the two spiral arms in the numerical solution in the $t = 16.66$ and 25.0 panels. Also, we note the numerical solution seems to exhibit a somewhat more pronounced broadening of the spiral bands. We speculate that nonlinear interactions between the developing azimuthal modes, which our theoretical work is not able to describe, is responsible for the difference.

In figure 8 we present a sequence of grey scale plots of the upper layer topographic Rossby wave field. The individual panels are in the Nof frame of reference and have the same horizontal domains, times and grey scale as in figure 5. The coordinate range in each panel corresponds to the translating sub-domain of the computational domain given by $-30 + t \leqslant x \leqslant 10 + t$ and $-20 \leqslant y \leqslant 20$.

The $t = 0$ panel in figures 5 and 8 are, of course, identical. The basic underlying pattern of crescent-shaped regions behind the cyclonic core with little, if any, wave field in the region ahead of the cyclonic core is the same in both figures 5 and 8. However, as time evolves, one can see the development of a higher azimuthal structure in the wave field behind the cyclonic core. This structure is the result of the time-dependent wave field which is excited in the upper layer due to the lower layer azimuthal anomalies. These variations can clearly be seen in the $t = 8.33$, 16.66 and 25.0 panels in both figures 5 and 8. The similarities in these variations is particularly striking in the first crest behind the cyclonic core in which there appears to be a local maximum developing near $y = 0$. The stretched appearance of the wave field in the along-slope direction ahead of the cyclonic core is a result of the damping associated with the numerical sponge layer.

Another aspect we can see in the numerical solution is the property of the point of maximum height to be offset from the centre of mass of the eddy. Indeed, as we will show in a moment, the point of maximum height precesses about the centre of mass very much like the theoretical solution predicts. While there are differences between the numerical simulation and our theory, it is obvious that nevertheless, qualitatively

https://doi.org/10.1017/S0022112098001049 Published online by Cambridge University Press

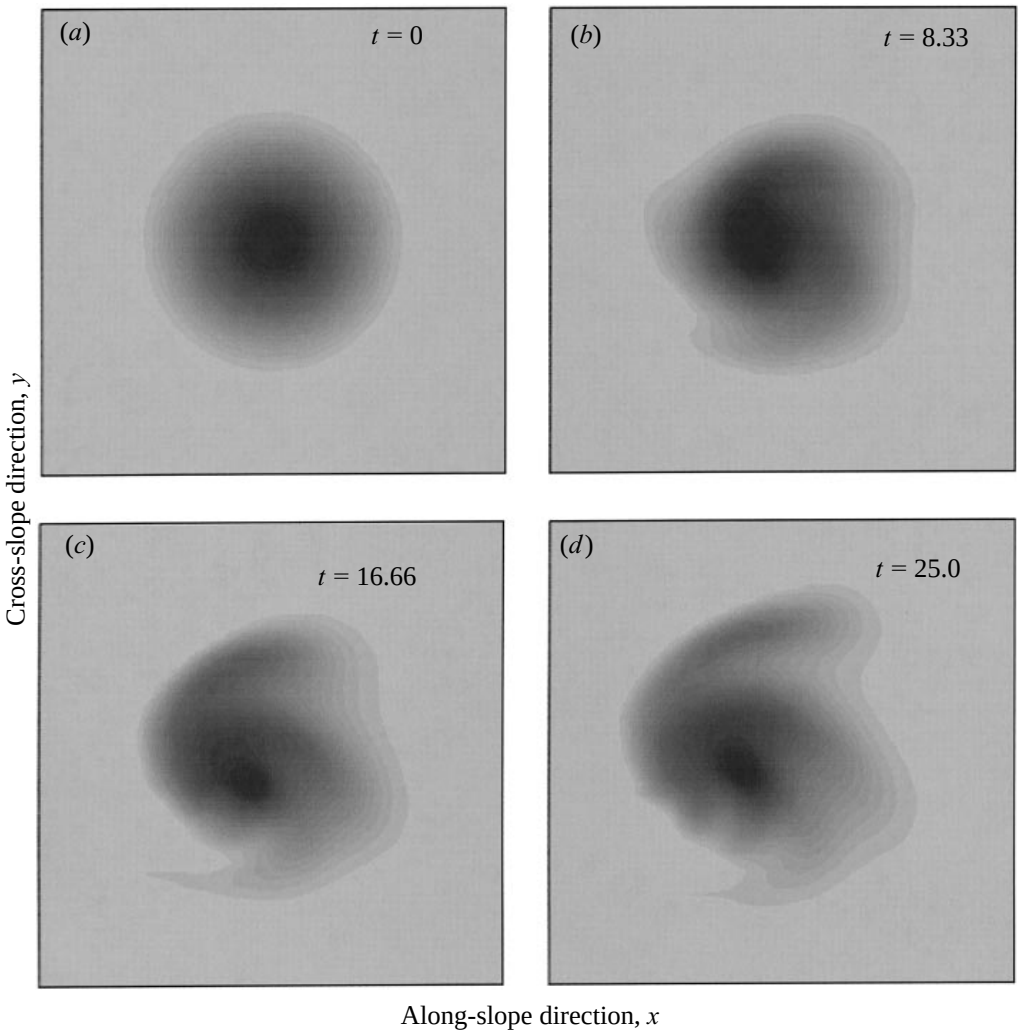


FIGURE 7. Sequence of horizontal grey-scale plots for the eddy height as determined by the numerical simulation. The domain, times and grey scale are the same as in figure 4.

at least, our approximate analysis has captured the dominant features of the spatial distortion of the cold dome.

It is also of interest to compute the centre of mass coordinates for the numerical simulation, which are given by

$$\langle xh \rangle_{num} = \frac{\iint_{\Omega_{num}} xh\,(x,y,t)\ \mathrm{d}x\mathrm{d}y}{\iint_{\Omega_{num}} h\,(x,y,t)\ \mathrm{d}x\mathrm{d}y}, \tag{5.6}$$

$$\langle yh \rangle_{num} = \frac{\iint_{\Omega_{num}} yh\,(x,y,t)\ \mathrm{d}x\mathrm{d}y}{\iint_{\Omega_{num}} h\,(x,y,t)\ \mathrm{d}x\mathrm{d}y}. \tag{5.7}$$

https://doi.org/10.1017/S0022112098001049 Published online by Cambridge University Press

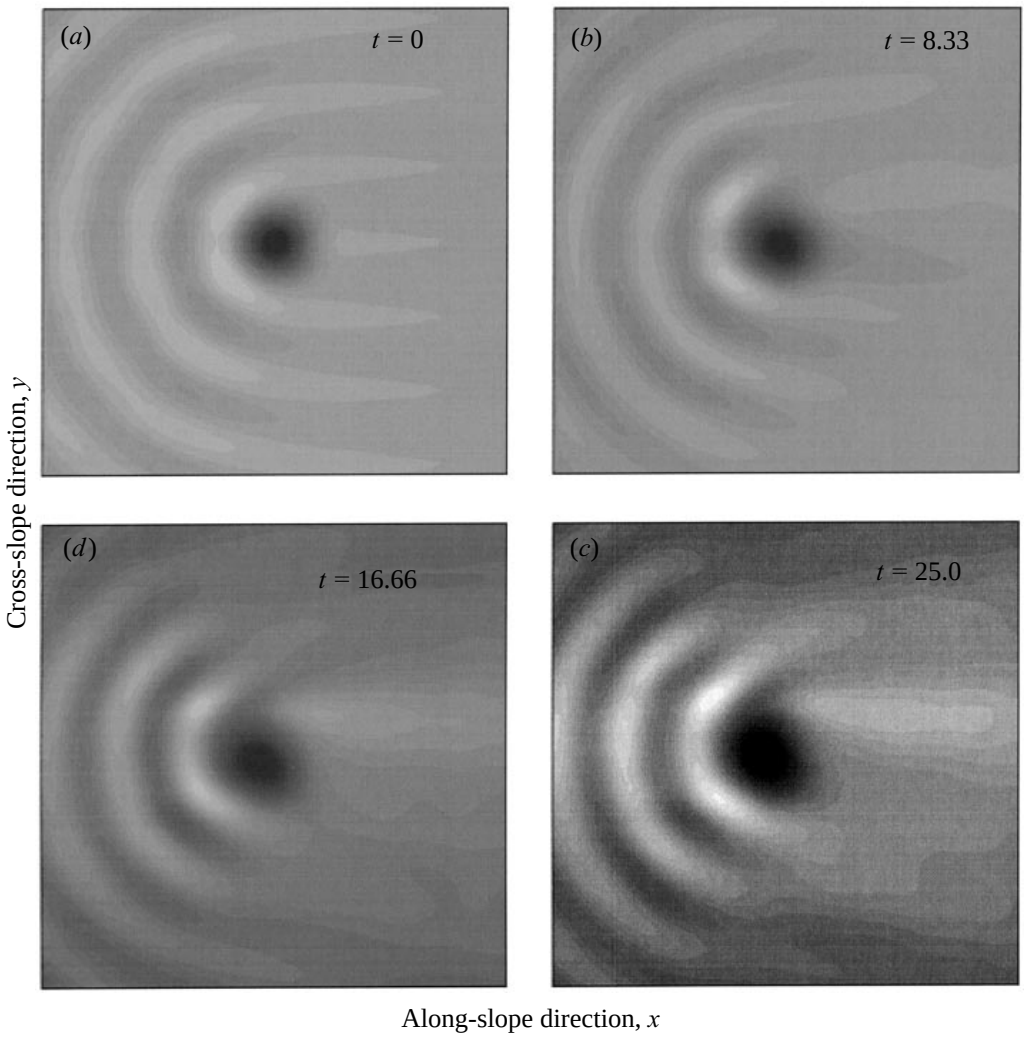


FIGURE 8. Sequence of horizontal grey-scale plots for the upper layer geostrophic pressure as determined by the numerical simulation. The times and grey-scale are the same as in figure 5.

We have introduced the subscript *num* to emphasize that these are computed from the numerical simulation over the computational domain. The integrals in (5.6) and (5.7) were evaluated using a trapezoidal rule. Since the grid spacing in both the x- and y-directions is approximately 0.47, this means that the error associated with the evaluation of the integrals is on the order of $0.47^2 \approx 0.2$.

In figure 9(a,b) we plot $\langle xh\rangle_{num}$ and $\langle yh\rangle_{num}$, respectively, as a function of the integration time. We see in figure 9(a) that $\langle xh\rangle_{num}$ suggests essentially rectilinear along-slope mass flux. A least-squares fit of the data points for $\langle xh\rangle_{num}$ gives a slope of about 0.95 which is within 5% of the Nof speed. This is consistent with our theoretical prediction for the along-slope velocity of the centre of mass.

After an initial adjustment, we see in figure 9(b) that $\langle yh\rangle_{num}$ varies in a predominately linear manner with time as suggested by our theoretical result (4.6). A least-squares fit of the data points after the initial adjustment period gives a slope of about 0.03. This is remarkably consistent with our theoretical result for the cross-

https://doi.org/10.1017/S0022112098001049 Published online by Cambridge University Press

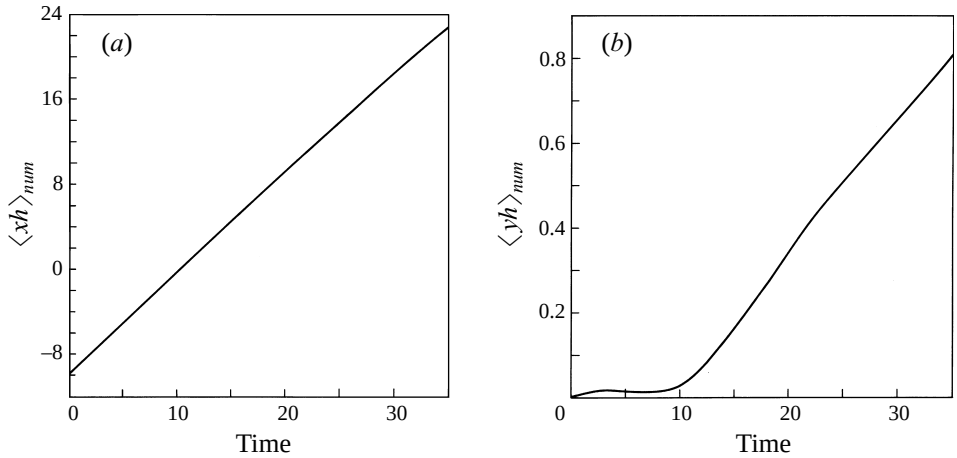


FIGURE 9. (*a*) The along-slope and (*b*) cross-slope centre of mass coordinates, respectively, for the numerical simulation.

slope centre of mass velocity $\partial_t Y_{mass} \simeq 0.01$ as determined in §4 given the order of magnitude of the errors associated with computing $\langle yh \rangle_{num}$.

We were also able to diagnose the position, denoted as $(\widetilde{X}_{max}, Y_{max})$, and magnitude, denoted as h_{max}, of the maximum height in the cold dome. The maximum was initially identified by searching the lower layer height computational array for the maximum value and then determined a precise value and location for the maximum by quadratic interpolation. Note that we have introduced a tilde in our notation for the numerically determined along-slope position in order to differentiate it from the notation used in our theoretical work in §4. In the theoretical work, X_{max} is the along-slope position relative to a frame of reference moving with the Nof velocity whereas here $\widetilde{X}_{max}$ denotes the position in a geostationary reference frame (we expect, of course, that $\widetilde{X}_{max} \approx t + X_{max}$).

In figure 10(*a*) we present a plot of the along-slope coordinate of the maximum height. The linear trend reflects the dominate contribution associated with the Nof velocity. This figure is very similar to figure 3(*c*).

In order to determine the along-slope position relative to the underlying linear trend we computed a least-squares fit to $\widetilde{X}_{max}$ and formed the residual along-slope position, i.e., $\widetilde{X}_{max}$ minus the least-squares fit. The residual along-slope position is the computational analogue of X_{max} as determined in the theoretical analysis.

The residual $\widetilde{X}_{max}$ as a function of time is shown in figure 10(*b*). The similarity between figures 10(*b*) and 3(*a*) is obvious. Both curves show a similar oscillatory pattern. Indeed, some of the details are in close agreement. In both figures the minimum and maximum occur at reasonably similar times. The peak to trough amplitudes of the oscillations are very similar too. This agreement is made even more striking when one realizes that the underlying asymptotic parameter $\mu \simeq 0.36$ which can hardly be described as vanishingly small.

In figure 10(*c*) we show the cross-slope position of the maximum height versus time. Again, we see that there is great deal of similarity between figure 10(*c*) and its theoretical counterpart figure 3(*b*). Note that the position of the first maximum and the following minimum occur at roughly the same times. Whereas the peak to trough amplitude of the oscillation in figure 3(*b*) is about 1.0, in figure 10(*c*) it is about 1.5.

https://doi.org/10.1017/S0022112098001049 Published online by Cambridge University Press

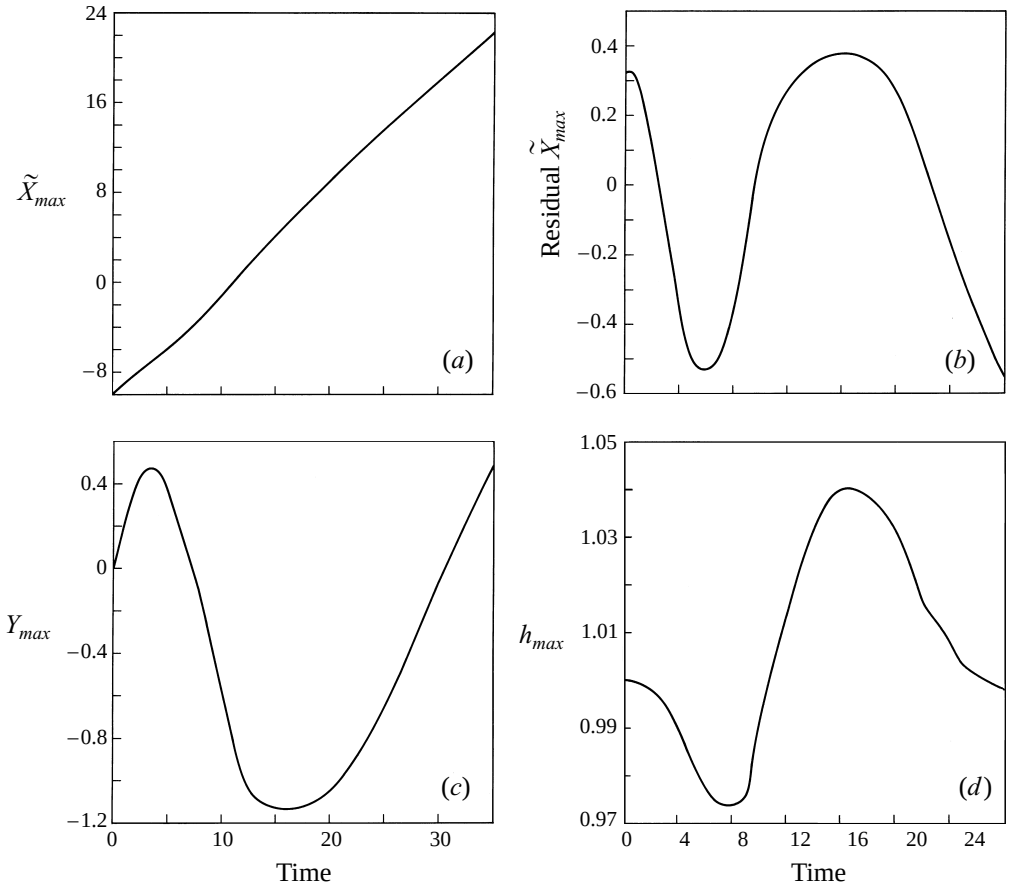


FIGURE 10. The coordinates of the maximum cold dome height as determined in the numerical simulation: (*a*) the along-slope position of the maximum height in geostationary coordinates versus time, (*b*) the residual along-slope position of the maximum total eddy height, i.e., with the linear trend removed, and (*c*) the cross slope position of the maximum height, versus time, respectively. (*d*) The value of the maximum height versus time.

The larger amplitude oscillation in figure 10(*c*) reflects the enhanced dilation of the cold dome seen in the numerical simulation as shown in figure 7.

In figure 10(*d*) we show h_{max} as a function of integration time for the numerical simulation. The period and peak to trough amplitude of the oscillations agrees favourably with the theory, i.e. figure 3(*d*). The numerical simulation suggests, however, that h_{max} decreases first and then begins to oscillate while the theory suggests that h_{max} experiences an initial increase and then begins to oscillate. Nevertheless, we are encouraged by the qualitative similarity between the oscillations in the two figures even though there appears to be a slight initial discrepancy.

6. Conclusions

In this paper we have developed a theory for the dynamical baroclinic interaction between a density-driven cold dome and a topographic Rossby wave field. The basic model we use is the two-layer one developed by Swaters & Flierl (1991) and Swaters (1991). This model describes the low-frequency dynamics of gravity-driven benthic

https://doi.org/10.1017/S0022112098001049 Published online by Cambridge University Press

currents on a sloping bottom within the context of allowing finite-amplitude variations in the lower layer eddy height while filtering out barotropic instabilities.

In general, the interaction between a topographic Rossby wave field and a cold dome is a fully nonlinear dynamical process. However, in the limit where the Mory–Stern isolation constraint (Mory 1985; Mory *et al.* 1987) is zero, there exists a radially symmetric isolated eddy configuration (see e.g. Swaters & Flierl 1991). Radially symmetric solutions possess the property that the nonlinear Jacobian terms in the governing equations are themselves identically zero. Here, we exploited this observation to examine the evolution of an eddy–topographic Rossby wave configuration for which the initial eddy height nearly satisfies the Mory–Stern isolation constraint. This allows the introduction of an asymptotic parameter which we can use to effectively linearize the dynamical interaction since the amplitude of the topographic Rossby wave field is proportional to the magnitude of the Mory–Stern isolation constraint.

There were a number of issues which motivated this study. Swaters (1998) recently described numerical simulations for the baroclinic instability of density-driven coupled fronts on a sloping bottom. These simulations showed that the spatial structure of the instabilities had the property that the perturbations to the down-slope incropping are preferentially amplified compared to those on the up-slope incropping. This asymmetry results in the formation of down-slope propagating plumes which eventually evolve into relatively coherent along-slope propagating cold domes.

Swaters (1998) analysed the propagation characteristics of these cold domes. In particular, the path followed by the point of maximum eddy height was composed of cross- and along-slope sub-inertial oscillations superimposed on a dominant along-slope drift reasonably well described by the Nof velocity (Nof 1983). The theory presented here is able to reproduce these oscillations. These oscillations form because the leading-order interaction between the eddy and exterior topographic Rossby wave field results in azimuthally propagating anomalies within the cold dome with radially dependent phase speeds which result in the point of maximum height precessing about the centre of mass relative to a frame of reference moving with the Nof velocity. To the level of approximation accounted for here, however, the centre of mass itself follows a steady trajectory in which the along-slope position is that predicted the Nof velocity and the cross-slope position monotonically increases in the down-slope direction. We also presented a numerical simulation of the governing equations for an initially weakly radiating cold dome. The predictions of our analytical work are remarkably similar to properties observed in the simulation.

Our results and methods should be relevant for other Rossby–wave eddy interaction problems. Previous attempts to determine the trajectory of, for example, the centre of mass of a warm-core ring have been based on attempting to derive a closed set of ordinary differential equations for the first-order spatial moments of the eddy height. In the barotropic situation this approach is successful (e.g. Zabusky & McWilliams 1982; Killworth 1983; Nof 1984). However, in the baroclinic context, this approach fails since, in general, it is not known how to parameterize the baroclinic stresses in terms of the eddy moments (Cushman-Roisin *et al.* 1990).

Our approach was not based on attempting to determine a parameterization of the baroclinic stresses in terms of the eddy height, but on explicitly calculating the time evolution of the baroclinic stresses within the aforementioned asymptotic approximation of a weak initial topographic Rossby wave field. Indeed, this asymptotic approach appears to be relevant. Numerical simulations presented by Swaters (1998) for an initial eddy configuration which does not satisfy the Mory–Stern isolation shows that these eddy solutions possess a perhaps surprisingly strong tendency to

https://doi.org/10.1017/S0022112098001049 Published online by Cambridge University Press

remain coherent over many eddy circulation times. This suggests that the asymptotic methods introduced here might be able to be profitably used to investigate other eddy–Rossby wave interactions.

Preparation of this manuscript was supported in part by Research Grants awarded by the Natural Sciences and Engineering Research Council of Canada.

REFERENCES

Arakawa, A. 1966 Computational design for long term numerical integration of the equations of fluid motion: two-dimensional incompressible flow. *J. Comput. Phys.* **1**, 119–143.

Armi, L. & D'Asaro, E. 1980 Flow structures in the benthic ocean. *J. Geophys. Res.* **85**, 469–483.

Asselin, R. A. 1972 Frequency filter for time integrations. *Mon. Wea. Rev.* **100**, 487–490.

Chapman, D. C. & Gawarkiewicz, G. 1995 Offshore transport of dense shelf water in the presence of a submarine canyon. *J. Geophys. Res.* **100** (C7), 13373–13387.

Cushman-Roisin, B., Chassignet, E. P. & Tang, B. 1990 Westward motion of mesoscale eddies. *J. Phys. Oceanogr.* **20**, 758–768.

Flierl, G. R. 1984 Rossby wave radiation from a strongly nonlinear warm eddy. *J. Phys. Oceanogr.* **14**, 47–58.

Gawarkiewicz, G. & Chapman, D. C. 1995 A numerical study of dense water formation and transport on a shallow, sloping continental shelf. *J. Geophys. Res.* **100** (C3), 4489–4507.

Griffiths, R. W., Killworth, P. D. & Stern, M. E. 1982 Ageostrophic instability of ocean currents. *J. Fluid Mech.* **117**, 343–377.

Houghton, R. W., Schlitz, R., Beardsley, R. C., Butman, B. & Chamberlin, J. C. 1982 The middle Atlantic bight pool: evolution of the temperature structure during 1979. *J. Phys. Oceanogr.* **12**, 1019–1029.

Jiang, L. & Garwood Jr., R. W. 1995 A numerical study of three-dimensional dense bottom plumes on a Southern Ocean continental slope. *J. Geophys. Res.* **100** (C9), 18471–18488.

Jiang, L. & Garwood Jr., R. W. 1996 Three-dimensional simulations of overflows on continental slopes. *J. Phys. Oceanogr.* **26**, 1214–1233.

Karsten, R. H., Swaters, G. E. & Thomson, R. E. 1995 Stability characteristics of deep-water replacement in the Strait of Georgia. *J. Phys. Oceanogr.* **25**, 2391–2403.

Killworth, P. D. 1983 On the motion of isolated lenses on a beta-plane. *J. Phys. Oceanogr.* **13**, 368–376.

LeBlond, P. H., Ma, H., Doherty, F. & Pond, S. 1991 Deep and intermediate water replacement in the Strait of Georgia. *Atmos.-Ocean* **29**, 288–312.

Miles, J. W. 1968 Lee waves in stratified flow. Part 2. Semi-circular obstacle. *J. Fluid Mech.* **33**, 803–814.

Mory, M. 1985 Integral constraints on bottom and surface isolated eddies. *J. Phys. Oceanogr.* **15**, 1433–1438.

Mory, M., Stern, M. E. & Griffiths, R. W. 1987 Coherent baroclinic eddies on a sloping bottom. *J. Fluid Mech.* **183**, 45–62.

Nof, D. 1983 The translation of isolated cold eddies on a sloping bottom. *Deep-Sea Res.* **30**, 171–182.

Nof, D. 1984 Oscillatory drift of deep cold eddies. *Deep-Sea Res.* **31**, 1395–1414.

Ou, H. W. & Houghton, R. 1982 A model of the summertime progression of the cold-pool temperature in the Middle Atlantic Bight. *J. Phys. Oceanogr.* **12**, 1030–1036.

Paldor, N. & Killworth, P. D. 1987 Instabilities of a two-layer coupled front. *Deep-Sea Res.* **34**, 1525–1539.

Smith, P. C. 1976 Baroclinic instability in the Denmark Strait overflow. *J. Phys. Oceanogr.* **6**, 355–371.

Swaters, G. E. 1991 On the baroclinic instability of cold-core coupled density fronts on a sloping continental shelf. *J. Fluid Mech.* **224**, 361–382.

Swaters, G. E. 1993 Nonlinear stability of intermediate baroclinic flow on a sloping bottom. *Proc. R. Soc. Lond.* A **442**, 249–272.

Swaters, G. E. 1998 Numerical simulations of the baroclinic dynamics of density-driven coupled fronts and eddies on a sloping bottom. *J. Geophys. Res.* **103**, 2945–2961.

https://doi.org/10.1017/S0022112098001049 Published online by Cambridge University Press

Swaters, G. E. & Flierl, G. R. 1991 Dynamics of ventilated coherent cold eddies on a sloping bottom. *J. Fluid Mech.* **223**, 565–587.

Whitehead, J. A., Stern, M. E., Flierl, G. R. & Klinger, B. 1990 Experimental observations of a baroclinic eddy on a sloping bottom. *J. Geophys. Res.* **95**, 9585–9610.

Whitehead, J. A. & Worthington, L. U. 1982 The flux and mixing rates of Antarctic Bottom Water within the North Atlantic. *J. Geophys. Res.* **87**, 7903–7924.

Visbeck, M., Marshall, J. & Haine, T. 1997 Specification of eddy transfer coefficients in coarse-resolution ocean circulation models. *J. Phys. Oceanogr.* **27**, 381–402.

Zabusky, N. J. & McWilliams, J. C. 1982 A modulated point vortex model for geostrophic, β-plane dynamics. *Phys. Fluids* **25**, 2175–2182.

Zoccolotti, L. & Salusti, E. 1987 Observations on a very dense marine water in the Southern Adriatic Sea. *Continent. Shelf Res.* **7**, 535–551.

https://doi.org/10.1017/S0022112098001049 Published online by Cambridge University Press